# Multiple parameters enable deconvolution of water-rock reaction paths in low-temperature vent fluids of the Kama ehuakanaloa (Lō ihi) seamount

Vincent Milesi, Everett Shock, Jeffrey Seewald, Elizabeth Trembath-Reichert, Sean P Sylva, Julie A Huber, Darlene S.S. Lim, Christopher R German

# MULTIPLE PARAMETERS ENABLE DECONVOLUTION OF WATER-ROCK REACTION PATHS IN LOW-TEMPERATURE VENT FLUIDS OF THE KAMA'EHUAKANALOA (LŌ'IHI) SEAMOUNT

Vincent Milesi[1,2,3*], Everett Shock[1,2,4], Jeffrey Seewald[5], Elizabeth Trembath-Reichert[2,5], Sean P. Sylva[5], Julie A Huber[5], Darlene S. S. Lim[6] and Christopher R. German[7]

[1]Group Exploring Organic Processes In Geochemistry, Arizona State University, Tempe, Arizona, 85287, USA

[2]School of Earth and Space Exploration, Arizona State University, Tempe, Arizona, 85287, USA

[3]Institut des Sciences de la Terre d'Orléans, Université d'Orléans, 45100, France

[*]vincentmilesi@hotmail.fr

[4]School of Molecular Sciences, Arizona State University, Tempe, Arizona, 85287, USA

[5]Marine Chemistry and Geochemistry, Woods Hole Oceanographic Institution, Woods Hole, Massachusetts 02543, USA

[6]Space Science and Astrobiology, NASA Ames Research Center, Moffett Field, California 94035, USA

[7]Geology and Geophysics, Woods Hole Oceanographic Institution, Woods Hole, Massachusetts 02543, USA

Key words: hydrothermal vents; active intraplate volcano; low-temperature vent fluids; fluid geochemistry; water-rock reactions; geochemical modeling; ocean Fe budget

## Highlights

- New data for vent-fluid compositions at Kama‘ehuakanaloa including $CO_2$ and $CH_4$ concentrations
- Persistent vent-fluid composition for three decades
- Geochemical modeling of water-rock-gas reactions that produce the 20-50 ºC vent fluids
- Low-temperature basalt alteration results in high Fe/low $H_2S$ vent fluids
- Key role of active intraplate volcanoes on ocean Fe-cycle


## Abstract

The contribution of venting fluids at mid-ocean ridges to global ocean biogeochemical cycles is well recognized. Less is known about the role of magmatically-active intra-plate volcanoes. In this study, new compositional fluid data were acquired from 20-50 ºC vent fluids at Kama‘ehuakanaloa (previously known as Lō‘ihi) seamount (Hawai’ian archipelago) and used to model the wide diversity of reaction conditions capable of producing the Fe-, Si- and $CO_2$-rich vent fluids observed. Our conceptual model includes a first step where seawater reacts with increasing proportions of basalt and gas as the temperature increases, and a second step where the resulting hydrothermal fluid mixes with unaltered seawater while continuing to react with basalt until the fluid mixture reaches 20 ºC. A series of reaction paths were chosen to vary: the maximum temperature during Step 1 (50 to 400 ºC) and the proportions of basalt and gas reacting; the degree, *F*, of low-temperature basalt alteration during Step 2, which corresponds to the extent to which the hot fluid generated during Step 1 continues to react with more basalt as it ascends to the seafloor. Our model shows that the 20-50 ºC vent fluids are greatly dependent on the degree of low-temperature basalt alteration during fluid upwelling. Indeed, the compositions of Kama‘ehuakanaloa vent fluids cannot be reconciled with a general model of subsurface mechanical mixing of high-temperature end-member vent fluid and seawater alone. Instead, they require both subsurface equilibrium mixing between a ≥350 ºC hydrothermal

fluid end-member and seawater and further basalt alteration that must occur as the fluid mixture rises to the seafloor. Although it involves only ~4% of the amount of basalt having reacted during Step 1, this low-temperature basalt alteration during Step 2 leads to the characteristic enrichments in Fe observed in the Kama‘ehuakanaloa vent fluids and a concomitant depletion in $H_2S$. We hypothesize that low-temperature basalt alteration during an extended path of fluid upwelling through the subseafloor might arise as a direct consequence of the height and steep-sloped topography of Kama‘ehuakanaloa seamount. If correct, this suggests a more general case - that input from magmatically-active intraplate volcanoes, which have been relatively overlooked throughout the history of submarine vent investigations to date, could differ significantly from global mid-ocean ridge fluxes and contribute more substantially than previously recognized to the global ocean Fe cycle.

## 1. Introduction

Hydrothermal circulation in the oceanic lithosphere plays a major role in global-scale ocean biogeochemical budgets (Edmond et al., 1979; German and Seyfried, 2014) and in supporting microbial life at and beneath the seafloor (e.g., Jannasch and Mottl, 1985; McCollom and Shock, 1997; Dick, 2019). Although hydrothermal activity at mid-ocean ridges has received much attention since its discovery in the late 1970's, that associated with active intraplate seamounts has been relatively overlooked (Beaulieu et al., 2015). Yet, new evidence reveals that such systems may sustain major biogeochemical fluxes to the ocean that need to be considered in global inventories (Bennett et al., 2011; Jenkins et al., 2020).

At the Kamaʻehuakanaloa seamount (previously known as Lōʻihi), the southernmost and youngest submarine volcano of the Hawai'ian hot-spot trace, it is well established that dissolved Fe released from low-temperature vent fluids produces redox disequilibria that support vast microbial communities dominated by iron-oxidizing bacteria (Emerson and Moyer, 2002; Emerson, 2009; Sylvan et al., 2017). During the GEOTRACES era, it has become apparent that dissolved Fe from mid ocean ridge hydrothermal venting can be traced long distances throughout every ocean basin (German et al., 2016). In the case of the South Pacific, it has been calculated that upwelling of this Fe into high nutrient low chlorophyll surface waters may account for ~30% of the drawdown of atmospheric $CO_2$ into the Southern Ocean (Resing et al., 2015). Only more recently has it been revealed, however, that dissolved Fe released from the Kamaʻehuakanaloa seamount may also persist sufficiently far as it disperses through the ocean to stimulate primary productivity in similar fashion in the high latitude North Pacific (Jenkins et al., 2020).

The Kamaʻehuakanaloa seamount is located 35 kms from the island of Hawai'i on the southern flank of Mauna Loa volcano and rises ~ 4 km above the abyssal plain to a depth of 950 m below sea level. Prior to the most recent eruptive activity in 1996, hydrothermal venting had been reported from the upper portion of the south rift zone; and on the east flank of the volcano as well as at its summit (Gamo et al., 1987; Sakai et al., 1987; Karl et al., 1988). After the eruption, venting was also established within a series of summit pit craters (Wheat et al., 2000; Glazer and Rouxel, 2009; Rouxel et al., 2018). Except for the

one-year survey period following the 1996 eruptive activity where temperatures up to 200 ºC were reported (Wheat et al., 2000), the vent fluids temperatures measured at Kamaʻehuakanaloa through a series of expeditions between 1987 and 2018 were mostly between 20 and 50 ºC. At these temperatures, the vent fluids exhibit pH values from 5.5 to 6.2 and are enriched in Si, Fe, $CO_2$, $NH_4^+$, $PO_4^{2-}$ and Mn and depleted in $H_2$ and $H_2S$ relative to mid-ocean ridge hydrothermal systems (Karl et al., 1988; Sedwick et al., 1992; Wheat et al., 2000; Glazer and Rouxel, 2009; Rouxel et al., 2018). The associated hydrothermal deposits consist of yellow-brown, well-crystallized goethite and smectite ranging in composition from Fe-montmorillonite to nontronite (Malahoff et al., 1982; De Carlo et al., 1983). This is quite distinct from basalt-hosted mid-ocean ridge hydrothermal systems where high temperature (~350 ºC) black smoker fluids enriched in $H_2S$ and variable amounts of chalcophile transition metals (e.g., Cu, Zn, Pb) result in the formation of polymetallic massive sulfide mounds (German and Von Damm, 2006).

Sedwick et al. (1992) proposed that pre-eruption Kamaʻehuakanaloa vent fluids resulted from a two-component subsurface mixing of seawater with a >350 ºC hydrothermal fluid endmember produced from water-rock-gas interactions. In that interpretation, the high Fe concentrations of the vent fluids resulted from the leaching of basalt walls by the resulting $CO_2$-rich vent-fluid mixture during upwelling to the seafloor. But the process, as discussed by Sedwick et al. (1992), could also explain the origin of the Sr isotope signature and Si and alkali metal enrichments of the vent fluids that would otherwise serve as evidence for a hot (>350 ºC) hydrothermal fluid endmember. Thus, the origin of Kamaʻehuakanaloa vent fluids and, especially, the relative contribution of low- and high-temperature water-rock interactions has never been fully resolved. Here we provide a quantitative evaluation of the water-rock-gas interactions at Kamaʻehuakanaloa to improve our understanding of the contribution that venting fluids associated with active intraplate seamounts could make to global-scale ocean biogeochemical budgets.

Specifically, we use newly collected geochemical data to calculate a series of reaction paths for water-rock-gas interactions associated with hydrothermal circulation and explore the diversity of reaction conditions capable of producing the low-temperature vent-fluid compositions observed at

Kama‘ehuakanaloa. Data were acquired during the 2018 SUBSEA expedition aboard the *E/V Nautilus* to the Kama‘ehuakanaloa seamount (Lim et al., 2019), to build upon earlier time-series and augment them with new data for dissolved $CO_2$ and $CH_4$ concentrations. Our study demonstrates how the chemical composition of low-temperature vent fluids can be used as a guide to water-rock reactions occurring at low-temperature in the shallow subsurface, and how those fluid compositions can be influenced by preceding water-rock reactions at higher temperatures. Our model results reveal a combination of parameters that can produce metal depletion or enrichment in low-temperature vent fluids which, in turn, can set export fluxes to the global ocean.

## 2. Material and Methods

### 2.1. Sampling and measurement

From August 21 to September 12, 2018, an exploratory mission to the Kama‘ehuakanaloa seamount was conducted aboard the *E/V Nautilus* as part of the SUBSEA research program. The Remotely Operated Vehicle *Hercules*, equipped with Isobaric Gas-Tight (IGT) sampling devices (Seewald et al., 2002), was used to collect duplicate fluid samples at 6 vents for a total of 12 samples. The pH (25 ºC) value, the alkalinity and the $CH_4$ and $H_2$ concentrations, which are time-sensitive analyses, were measured onboard daily. A Gas Chromatograph (GC) equipped with a Thermal Conductivity Detector (TCD) and a Flame Ionization Detector (FID) was used to measure $H_2$ and $CH_4$, respectively, with detection limits of 3 $\mu$M and 0.05 $\mu$M. $H_2S$ concentrations were below the detection limits of the analytical method of Cline (1969) available onboard ship, i.e., <1 µM. At the Woods Hole Oceanographic Institution laboratory, major cations and anions were analyzed with inductively coupled plasma mass spectrometry (ICP-MS) and ion chromatography. Concentrations reported for major cations are from ICP-MS except for Ca for which interference with $^{40}Ar^{+}$ prevents accurate measurements. GC-TCD was used to measure total dissolved inorganic carbon (DIC) as $CO_2$ after acidification of samples with a 25 wt.% phosphoric acid solution.

### 2.2. Modeling

Geochemical modeling was performed with the EQ3/6 geochemical software (Wolery, 2010) using thermodynamic data for minerals and dissolved inorganic aqueous species from Helgeson et al. (1978), Shock and Helgeson (1988), Shock et al. (1989, 1992, 1997) and Sverjensky et al. (1997). The Gibbs free energies for clay minerals were estimated using the method of Wolery and Jove-Colon (2004). The other thermodynamic parameters (S, V, Cp) are from Helgeson et al. (1978). All modeling was performed in the system $Na_2O$-Cl-MgO-CaO-$K_2O$-$SiO_2$-$SO_2$-$CO_2$-$Al_2O_3$-FeO-CuO-ZnO-$TiO_2$. MnO was excluded from the modeling because the limited number of Mn-bearing minerals in our database prevents a realistic description of Mn behavior. The model used for the calculation of activity coefficients is based on the B-dot equation for electrically charged species (Helgeson, 1969). For neutral solute species, the activity coefficient is taken equal to that of aqueous $CO_2$ in pure sodium chloride solutions of the same ionic strength (Garrels and Thompson, 1962; Helgeson, 1969). Using this approach, the activity coefficient of neutral solute species increases with increasing ionic strength, which is consistent with the "salting out" effect.

Although the Kama'ehuakanaloa summit is 950 m below sea level, the subseafloor heat source could be much deeper as the volcano rises from >5000 m depth at its base. We considered a single constant pressure of 500 bars for all our calculations, which corresponds to a depth of ~5000 m below sea level. This assumption is reasonable because the pressure has relatively little effect on thermodynamic equilibria involving condensed phases and dissolved aqueous species compared to the effects of temperature. Our model assumptions hit their limits if phase separation were to occur due to a combination of high temperature (>400 ºC) and low pressure (<300 bars) (Bischoff and Rosenbauer, 1985), as might happen during eruptive events (Wheat et al., 2000).

Our conceptual model of water-rock reactions during hydrothermal circulation involves two reaction steps as illustrated in Figure 1. In Step 1, we quantify the results as seawater reacts in open systems with Kama'ehuakanaloa basalt while the temperature rises progressively and volcanic gases are added ($CO_2$, $SO_2$ and $H_2O$). In Step 2, the resulting high-temperature fluid is mixed with seawater in a second open system, while continuing to react with the basaltic interior of the volcano as it rises toward the summit,

until the fluid mixture reaches the temperature of 20 ºC. This scenario was chosen to account for the water-rock-gas reactions proposed by Sedwick et al. (1992) that produce the Kama‘ehuakanaloa vent fluids. In order to investigate a large range of possible reaction conditions varying in terms of temperature, rock/water ratios and gas inputs, we used the programming language Python to automate the multiple runs and data processing of model results following the approach of Ely (2020) and Milesi et al. (2021).

During Step 1, the temperature increases from 2 ºC to a temperature maximum (*Tmax*) ranging from 50 to 400 ºC, at intervals of 50 ºC (Figure 1a). The composition of seawater is taken from Bruland and Lohan (2006). Basalt composition at Kama‘ehuakanaloa includes tholeiitic, transitional and alkalic basalt as well as basanite (Moore et al., 1982; Dixon and Clague, 2001). On the upper portion of the south rift zone where the vent fields visited during the 2018 SUBSEA expedition are located, the basalt is moderately alkalic in composition, weakly phyric, containing 1-2 vol.% of olivine, plagioclase and augite, and becomes more tholeiitic going south (Karl et al., 1988). In our model, we used the basalt composition reported by Karl et al. (1988) at the Kama‘ehuakanaloa summit which falls within the compositional range described by Dixon and Clague (2001). The rock/water ratio (*R/W*) of Step 1, *i.e*., the mass of basalt in kilograms reacting with 1 kg of water, increases as the temperature maximum increases (Figure 1b), following the equation:

$$R/W_{Step1} = \frac{T_{max}}{350} \quad . \tag{1}$$

There is essentially an infinite number of temperature-rock/water ratio paths, only a few of which are considered through Equation (1). After several iterations, we settled on this particular path as it is consistent with previous practices and observational data (Bowers and Taylor, 1985). Especially, Equation (1) leads to a rock/water ratio of 1 at 350 ºC, consistent with literature estimates (Von Damm et al., 1985).

The Lo’ihi vent fluids are known to be impacted by magmatic degassing (Karl et al., 1988; Sedwick et al., 1992; Wheat et al., 2000); however, the timing of $CO_2$ and $SO_2$ inputs during hydrothermal circulation is unconstrained. Inputs of magmatic gas were considered to be a linear function of the primary

concentrations of volatiles in basalt and the rock/water ratio. Because $CO_2$, $SO_2$ and $H_2O$ are volatile species that tend to degas during eruption, their primary concentrations were reconstructed using ratios of volatile to non-volatile elements that may behave similarly during melting and crystallization (Michael, 1988; Saal et al., 2002; Aubaud, 2004; Cartigny et al., 2008; Rosenthal et al., 2015). The $CO_2$, $SO_2$, and $H_2O$ concentrations were reconstructed using Ba, Ce, and Dy concentrations, respectively (Saal et al., 2002; Rosenthal et al., 2015). Values of 133, 168 and 225 were adopted for the $CO_2$/Ba, $H_2O$/Ce and S/Dy ratios, respectively. The Ba, Ce and Dy concentrations for Kama‘ehuakanaloa basalt are from Dixon and Clague (2001) (Table S 1).

During Step 2 of the model, seawater at 2 ºC is added to the hydrothermal fluid endmember until the fluid mixture reaches 20 ºC (Figure 1a). Temperature is controlled only by mixing of the fluids, so that the addition of each increment of seawater lowers the temperature of the fluid mixture. As the temperature is lowered, proportionally greater amounts of seawater are required to lower the temperature further. Because the reaction progress of Step 2 is proportional to the amount of added seawater, most of the water-rock interaction occurs at low temperature, <50 ºC. The rock/water ratio of Step 2 is defined by:

$$R/W_{Step2} = F * R/W_{Step1} \quad (2)$$

where *F* (referred hereafter as the ‘degree of low-temperature basalt alteration’) is the fraction of basalt altered relative to Step 1 and was varied from 0 to 20% (Figure 1b). The small proportion of basalt reacting during Step 2 (*F*) compared to that reacting during the initial high-temperature reactions at depth (Step 1) is meant to account for rapid flow rates and temperature decreases from the temperature maximum reached during Step 1 as the fluids continue to upwell and mix. The proportion of gas reacting during Step 2 is calculated similarly as in Step 1.

Step 2 was modeled considering either equilibrium chemistry (referred to hereafter as ‘equilibrium mixing’) or non-equilibrium chemistry for which only aqueous speciation reactions proceed but redox reactions and mineral precipitation are suppressed (referred hereafter as ‘mechanical mixing’). The latter

case aims to account for possible disequilibrium between rapidly ascending high-temperature fluids, the rock, and the added seawater. During mechanical mixing, no low-temperature basalt alteration is considered as it would otherwise lead to unrealistically high solute concentrations. In our equilibrium calculation, methane is suppressed because the reduction of seawater-derived $CO_2$ during hydrothermal circulation within the oceanic crust is known to be kinetically inhibited (McDermott et al., 2015). Quartz and dolomite are also suppressed because kinetic limitations are expected to prevent their formation at low temperature, especially during Step 2 (Rimstidt and Barnes, 1980; Von Damm et al., 1991; Arvidson, 1999). After several iterations and for consistency with observational data, nontronite was also removed from our mineral database, leaving saponite, montmorillonite and beidellite among the minerals of the smectite-group that can form.

For all fluid samples, *in situ* pH values were calculated with EQ3 by speciating the fluid composition at 25 ºC and 1 bar with charge balance on chloride, then speciating the resulting fluid composition at the temperature of sampling (Reed and Spycher, 1984). Published data of vent-fluid composition are taken from prior studies by Karl et al. (1988), Sedwick et al. (1992, 1994), Hilton et al. (1998), Glazer and Rouxel (2009) and Rouxel et al. (2018). Sedwick et al. (1992) reported ranges of concentrations: only the maximum and minimum values from that work are considered in this study. Sedwick et al. (1994) and Hilton et al. (1998) reported only concentrations for dissolved silica and dissolved inorganic carbon, so no *in situ* pH was calculated from these data.

## 3. Results

### 3.1. Measured vent-fluid compositions

The location and chemical composition of the Kamaʻehuakanaloa vent fluids sampled during the 2018 SUBSEA expedition are shown in Table 1. The composition of the vent fluid sampled at Marker 34 is compared to seawater values and to the end-member compositions of vent fluids from hydrothermal systems in a variety of geologic environments on the seafloor in Table 2. Basalt-hosted hydrothermal systems on mid-ocean ridges are represented by the 21ºN East Pacific Rise (EPR) vent field, characterized

by 350ºC fluids exiting black smoker chimneys (Von Damm et al., 1985). Hydrothermal systems in back-arc basins associated with felsic volcanic rocks are represented by the Mariner vent field located along the Eastern Lau Spreading Center. There, input of acidic volatiles ($CO_2$, $SO_2$, HCl and HF) in the circulating hydrothermal fluids produces >350 ºC vent fluids with a low pH value (2.7) and high metal concentrations (Mottl et al., 2011). Ridge flank systems are represented by Baby Bare, an isolated seamount on the eastern flank of the Juan de Fuca Ridge where low-temperature (<100 ºC) hydrothermal reactions in the basement produce 25 ºC hydrothermal springs (Wheat and Mottl, 2000).

The temperature range of 15º to 41ºC measured during the 2018 SUBSEA expedition is comparable to that of Baby Bare springs (25 ºC) and much lower than the temperatures that characterize vent fluids at 21ºN EPR and Mariner. The pH (25 ºC) values ranging from 5.4 to 6.2 at Kamaʻehuakanaloa are lower than at Baby Bare but higher than the values of 3.4 and 2.7 in 21ºN EPR and Mariner vent fluids, respectively. One of the most striking features of the Kamaʻehuakanaloa vent fluids is the high values of alkalinity up to 14.3 meq/kg whereas alkalinity values in the 21ºN EPR, Mariner, and Baby Bare vent fluids are either negative or close to 0. In comparison to the other vent fluids, the Cl, sulfate, Na, K and Mg concentrations at Kamaʻehuakanaloa are relatively close to seawater values. In the Spillway and Lohiau areas, the Kamaʻehuakanaloa vent fluids are slightly depleted in Mg and sulfate but to a much lower extent that what is observed in the 21ºN EPR, Mariner, and Baby Bare vent fluids. With concentrations up to 16.3 mmol/kg, Ca can be enriched at Kamaʻehuakanaloa relative to seawater, but the enrichment is less than at Mariner and Baby Bare. The Si concentration up to 2.8 mmol/kg at Kamaʻehuakanaloa is 5 to 10 times higher than seawater and Baby Bare values but it is lower than that of the >350 ºC vent fluids. Similarly, Fe and Mn are enriched compared to seawater and Baby Bare springs, with concentrations up to 0.98 and 0.07 mmol/kg, respectively. These values are 1 to 2 orders of magnitude lower than at 21ºN EPR and Mariner. $CH_4$ at Kamaʻehuakanaloa is enriched compared to seawater but to a lesser extent than in black smoker systems, whereas $H_2$ and $H_2S$ are not detected. Finally, the $CO_2$ concentration ranging from 14 to 126

mmol/kg at Kama‘ehuakanaloa is one order of magnitude higher than in seawater and comparable to values of the Marnier vent field (Mottl et al., 2011).

New data for Kama‘ehuakanaloa vent-fluid compositions from the 2018 SUBSEA expedition are compared to previously published data for vent fluids sampled at the summit of the volcano (Karl et al., 1988; Sedwick et al., 1992, 1994; Hilton et al., 1998; Glazer and Rouxel, 2009; Rouxel et al., 2018) (Figure 2). This comparison indicates that overall, the composition and temperature of the vent fluids were relatively constant through time from 1988 to 2018 except for the short-lived event in 1996. Small variations exist for pH, Si, DIC and Fe concentrations but no trend with time is identified. The tectonic-volcanic event of July-August 1996 created a pit crater (Pele's Pit) and several sites of vigorous hydrothermal venting, with temperature up to 200 ºC measured in September 1997 (Davis and Clague, 1998; Wheat et al., 2000); however, subsequent exploratory dives over three cruises between 2006 and 2008 (Glazer and Rouxel, 2009; Rouxel et al., 2018) and the 2018 SUBSEA exploration reported temperatures (15-41 ºC, Table 1) and fluid compositions similar to pre-eruptive values (Karl et al., 1988; Sedwick et al., 1992, 1994).

As a hydrothermal fluid end-member mixes with seawater beneath the seafloor, the chemical signatures inherited from the water-rock-gas reactions can be progressively lost. The degree of loss depends on the involvement of chemical species in the water-rock-gas reactions and their concentrations in seawater. Therefore, we prioritized the use of Si, pH, DIC, Ca and Fe to constrain the geochemical models because these are the species that differ most from seawater values. Although $CH_4$ is also enriched relative to seawater, unambiguous information is less likely to be obtained from modelling this species distribution because its concentration can be the result of numerous processes including biogenic formation (e.g., Bradley and Summons, 2010), pyrolysis of organic matter (Welhan, 1988), kinetic limitations inhibiting abiotic formation and oxidation (McDermott et al., 2015, 2020) and leaching of fluid inclusions and gas vesicles (Klein et al., 2019; Grozeva et al., 2020).

*Table 1. Locations and chemical compositions of fluid samples collected during the 2018 SUBSEA expedition*

| Sample (NA100-) | 002 | 001 | 039 | 040 | 019 | 054 | 053 | 061 | 060 | 080 | 079 | 059 |
|---|---|---|---|---|---|---|---|---|---|---|---|---|
| Marker* | 34 | 34 | 38 | 38 | 31[g] | 2 | 2 | 57 | 57 | 57' | 57' | Bottom seawater |
| Site* (lat; long; depth (m)) | Spillway Area (18.906; -155.257; 1270±3) | | | | | Lohiau area (18.909; -155.257; 1179±2) | | Pohaku (18.901; -155.258; 1184±2) | | | | |
| Temperature max. (ºC)[a] | 41 | 41 | 39 | 37 | 31 | 22 | 21 | 15 | 18 | 21 | 21 | - |
| pH (25 ºC) | 5.8 | 6.0 | 6.0 | 6.1 | 6.0 | 6.2 | 6.2 | 5.4 | 5.7 | 5.7 | 5.7 | 7.4 |
| Alkalinity[b] (meq/kg) | 14.3 | 14.3 | 13.5 | 9.2 | 8.4 | 8.8 | 8.9 | 6.5 | 11.6 | 13.6 | 12.9 | 2.3 |
| Na (mmol/kg) | 459 | 463 | 464 | 460 | 462 | 490 | 464 | 465 | 463 | 466 | 464 | - |
| Cl[b] (mmol/kg) | - | 545 | 545 | 542 | 544 | 541 | 543 | 540 | 538 | 537 | 538 | 539 |
| Mg (mmol/kg) | 51.5 | 51.5 | 52.0 | 52.2 | 50.0 | 52.5 | 52.8 | 54.0 | 55.0 | 54.7 | 54.5 | - |
| Ca[b] (mmol/kg) | 15.1 | 15.8 | 15.3 | 14.3 | 14.9 | 16.0 | 16.3 | 10.9 | 11.3 | 11.4 | 10.6 | 10.3 |
| K (mmol/kg) | 12.2 | - | 12.1 | 11.3 | 12.4 | 16.6 | 11.4 | 10.7 | 11.1 | 11.7 | 11.7 | - |
| Sulfate (mmol/kg)[c] | 27.0 | 26.7 | 26.9 | 27.3 | 25.8 | 27.0 | 27.0 | 27.9 | 27.3 | 26.6 | 26.8 | 28.2 |
| Si (mmol/kg) | 2.8 | 2.7 | 2.7 | 1.5 | 1.9 | 1.7 | 1.5 | 0.6 | 1.4 | 1.8 | 1.9 | - |
| Fe (µmol/kg) | 413 | 517 | 579 | 289 | 384 | 369 | 285 | 308 | 758 | 980 | 978 | 0 |
| Mn (µmol/kg) | 40 | 40 | 38 | 24 | 25 | 73 | 45 | 10 | 18 | 21 | 22 | - |
| Al (µmol/kg) | n.d. | n.d. | n.d. | n.d. | n.d. | n.d. | n.d. | n.d. | n.d. | n.d. | n.d. | - |
| Sr (µmol/kg) | 104 | 103 | 103 | 95 | 98 | - | 102 | 87 | 88 | 87 | 87 | - |
| Ba (µmol/kg) | 0.7 | 0.7 | 0.9 | 0.7 | 0.9 | - | 0.7 | 0.7 | 1.0 | 0.6 | 1.0 | - |
| B (µmol/kg) | 398 | 402 | 424 | 410 | 398 | 553 | 388 | 424 | 452 | 491 | 484 | - |
| Li (µmol/kg) | 53 | 53 | 52 | 42 | 44 | 76 | 40 | 32 | 38 | 45 | 45 | - |
| Rb (µmol/kg) | 5.0 | 4.9 | 4.7 | 3.3 | 4.6 | 5.8 | 3.5 | 2.0 | 2.8 | 3.4 | 3.4 | - |
| Cs (µmol/kg) | 0.24 | 0.24 | 0.26 | 0.23 | 0.26 | 0.48 | 0.24 | 0.24 | 0.24 | 0.24 | 0.25 | - |
| Cu (µmol/kg) | 0.9 | 1.1 | 1.4 | 5.3 | 1.6 | 6.4 | 0.5 | 1.6 | 1.3 | 0.9 | 1.8 | - |
| Zn (µmol/kg) | 27.6 | 27.9 | 7.7 | 6.0 | 32.5 | 134.4 | 12.4 | 22.9 | 4.3 | 4.0 | 14.2 | - |
| $H_2$ (µmol/kg)[d] | <3 | <3 | <3 | <3 | <3 | <3 | <3 | <3 | <3 | <3 | <3 | - |
| $CO_2$ (mmol/kg)[d] | 31.2 | 31.2 | 30.0 | 18.3 | 17.4 | 14.2 | 14.0 | 43.8 | 94.1 | 124.3 | 125.8 | - |
| $CH_4$ (µmol/kg)[e] | 1.5 | 1.3 | 1.2 | 0.8 | 1.4 | 0.6 | 0.6 | 1.6 | 2.8 | 4.3 | 3.8 | - |
| $H_2S$ (µmol/kg)[f] | <1 | <1 | <1 | <1 | <1 | <1 | <1 | <1 | <1 | <1 | <1 | - |

*Marker and site from Rouxel et al. (2018)
[a]Temperature maximum recorded during the IGT sampling
Analysis with ICP-MS, unless otherwise noted: [b]Gran titration, [c]ion chromatography, [d]GC-TCD, [e]GC-FID, [f]spectrophotometry Cline (1969)
[g]Duplicate sample leaked
n.d. = not detected
Estimated uncertainties (2σ) are as follow: pH (25ºC) values ±0.1 unit; Na, Mg, Cl, Ca, K, sulfate concentrations ±3%; $SiO_2$, Fe, Mn, Sr, Ba, Li, Rb, Cs, Cu, Zn concentrations ±5%; $CH_4$ and $CO_2$ concentrations ±10% and ±5%, respectively.

*Table 2. Vent-fluid compositions from Kama'ehuakanaloa compared with submarine vent fields from various other geologic settings*

| Vent field | Seawater | Kama'ehuakanaloa [a] | 21ºN, EPR [b] | Mariner | Baby Bare (Spring water) |
|---|---|---|---|---|---|
| Geologic setting | - | Intraplate volcano | Mid ocean ridge | Back arc | Ridge flank |
| Max. T (ºC) | 2 | 41 | 350 | 363 | 25 |
| pH (25 ºC) | 7.8 | 5.9 | 3.4 | 2.7 | 8.3 |
| Alk. (meq/kg) | 2.3 | 14.3 | -0.4 | -2.25 | 0.43 |
| Cl (mmol/kg) | 546 | 546 | 489 | 605 | 554 |
| $SO_4$ (mmol/kg) | 28 | 26.9 | 0.5 | - | 17.8 |
| Na (mmol/kg) | 468 | 460.8 | 432 | 439 | 473 |
| K (mmol/kg) | 10.2 | 12.4 | 23 | 36.9 | 6.9 |
| Ca (mmol/kg) | 10.3 | 15.5 | 16 | 43.8 | 55.2 |
| Mg (mmol/kg) | 53 | 51.5 | 0 | 1.9 | 0.98 |
| Si (mmol/kg) | 0.1 | 2.8 | 18 | 15.1 | 0.4 |
| Fe (µmol/kg) | <0.001 | 465 | 1,664 | 12991 | <0.1 |
| Mn (µmol/kg) | <0.001 | 40 | 960 | 5723 | 7.8 |
| $CH_4$ (µmol/kg) | - | 1.4 | 70 | - | - |
| $H_2$ (mmol/kg) | - | b.d.l | 1.7 | - | - |
| $CO_2$ (mmol/kg) | - | 31.2 | 5.7 | 39.8 | 0.4 |

| | | | | | |
|---|---|---|---|---|---|
| $H_2S$ (mmol/kg) | - | b.d.l | 7.3 | 9.3 | - |

[a] Average values of the 2018 SUBSEA fluids sampled at Marker 34.
[b] Measured composition of vent fluids are corrected for entrainment of seawater during sampling based on the quantitative removal of Mg from the fluid during water-rock reactions.
Data are from Bruland et al. (2006) for seawater, Humphris and Klein (2017) for 21ºN EPR and Mariner vent fields (original data from Von Damm et al. (1985) and Mottl et al. (2011), respectively), Wheat and Mottl (2000) for Baby Bare.
Abbreviation: Max. T = maximum temperature; Alk. = Alkalinity; - = not determined; b.d.l = below detection limit.

## 3.2. Modeled fluid compositions

### 3.2.1.pH, Ca and DIC

Our calculations predict a wide diversity of fluid compositions over the range of Step 1 and Step 2 reaction conditions as shown in Figure 3. During Step 1, the increase of temperature and rock/water ratio results in a decrease of pH (Figure 3a). After a sharp increase, the Ca concentration decreases as well because of the precipitation of smectite, epidote and tremolite which fixes Ca (Figure 3b, Figure S 1 to Figure S 3 in supplementary information). The DIC concentration increases in parallel due to the inputs of $CO_2$ (Figure 3c), linearly correlated to the rock/water ratio (see section 2.2). As a result, the hydrothermal fluid is at equilibrium with calcite all along Step 1, except for temperatures above 350 ºC (Figure 3d).

At the beginning of the mixing between the hydrothermal fluid and seawater during Step 2, the pH value decreases drastically (Figure 3a). $H^+$ is produced by the precipitation of minerals in response to the supply of cations by seawater. As the mixing progresses and the temperature of the fluid mixture decreases, the pH values increase. Overall, the pH values of the 20 ºC fluids at the end of Step 2 decrease with the increase of Step 1 temperature maximum. In addition, there is an increase of pH with the degree of low-temperature basalt alteration during Step 2 as $H^+$ is consumed by basalt dissolution. This is especially pronounced in 20 ºC fluids produced by reaction paths with temperature maxima >300 ºC. Consequently, the diversity of pH values in the 20 ºC fluids decreases with the increase of low-temperature basalt alteration. For F values >7%, all reaction paths converge toward the same pH values at the end of Step 2, regardless of the temperature maximum reached during Step 1.

As mixing with seawater progresses during Step 2, the Ca concentrations in fluids produced by reaction paths with Step 1 temperature maxima >250 ºC increase whereas the DIC concentrations decrease

(Figure 3b and c). This trend is reversed for reaction paths with lower temperature maxima. Overall, the Ca and DIC concentrations in the 20 ºC fluids decrease and increase, respectively, as the temperature maximum in Step 1 increases. In addition, these concentrations increase with the degree of low-temperature basalt alteration because the dissolution of basalt supplies both Ca and $CO_2$. Although less apparent than in the case of pH, there is also a loss of diversity for the Ca and DIC concentrations of the 20 ºC fluids as low-temperature basalt alteration increases. For F values >7%, all reaction paths tend to produce similar Ca and DIC concentrations, independently of Step 1 reaction conditions.

The combined behavior of pH, Ca and DIC concentrations leads the fluid mixture to depart from equilibrium with calcite at the beginning of Step 2 before returning to saturation with calcite at high degrees of mixing at the end of Step 2 (Figure 3d). Equilibrium with calcite is especially common in 20 ºC fluids inherited either from reaction paths with low Step 1 temperature maxima or high degrees of low-temperature basalt alteration. By buffering the pH value of 20 ºC fluids produced by reaction paths with F values >7%, equilibrium with calcite causes a loss of chemical diversity. Therefore, the dependence of the 20 ºC fluid compositions on Step 1 and Step 2 reaction conditions relies on the capacity of the system to counterbalance the pH increase that leads to calcite saturation at the end Step 2. Two competing effects influence the evolution of pH: (1) high $CO_2$ supply and high-temperature mineral precipitation during Step 1 tend to lower the pH values of the resulting 20 ºC fluids, whereas (2) $H^+$ consumption by low-temperature basalt alteration tends to increase the pH values.

#### 3.2.2. Sulfate, Mg, K, Si, Na and Cl

During Step 1, the increase of temperature and rock/water ratio result in the decrease of sulfate and Mg concentrations as sulfur is fixed into pyrite and Mg into saponite (Figure 4a and b, Figure S 4 and Figure S 1 in supplementary information). After a sharp decrease, the K concentrations increase, controlled by the precipitation of muscovite at high temperature (Figure 4c, Figure S 5 in supplementary information). The Si concentrations increase reaching values close to equilibrium with quartz (Figure 4d, Figure S 6 in supplementary information).

During Step 2, mixing with seawater supplies sulfate and Mg to the fluid mixture (Figure 4a and b). The sulfate and Mg concentrations converge toward seawater values as mixing progresses such that the chemical signature inherited from the water-rock reactions during Step 1 and Step 2 is lost. The K concentrations progress as well toward the seawater value during Step 2, except for degrees of low-temperature basalt alteration > 7% (Figure 4c). In these cases, the fluid mixtures reach equilibrium with K-feldspar at the end of Step 2, the precipitation of which fixes K (Figure S 7 in supplementary information). For Si, the 20 ºC fluids retain the chemical signatures of the Step 1 and Step 2 reaction conditions (Figure 4d). The Si concentrations of the fluid mixtures at the end of Step 2 increase with Step 1 temperature maxima. For degrees of low-temperature basalt alteration > 7%, the diversity of Si concentrations in the 20 ºC fluids decreases, as observed for pH values, Ca and DIC concentrations.

The Cl and Na concentrations are marginally impacted by the reaction paths (Figure S 8 in supplementary information). Cl is not directly involved in the water-rock reactions and the consumption of $H_2O$ in the formation of hydrated minerals is low enough that the Cl concentration is not impacted significantly. Because of the high Na concentration in seawater, the relative impact of water-rock reactions such as albitization is low and erased by the mixing with seawater during Step 2.

#### 3.2.3.Fe and $H_2S$

As the temperature and rock/water ratio increase during Step 1, the water-rock reactions produce $H_2$ from the oxidation of ferrous iron in the basalt. Therefore, sulfate is reduced to $H_2S$, which increases in concentration such that the fluid reaches equilibrium with pyrite (Figure 5a, Figure S 4 in supplementary information). The concentration of Fe increases as well (Figure 5b), controlled by the precipitation of pyrite and Fe-chlorite (Figure S 4 and Figure S 9 in supplementary information).

The redox conditions in the 20 ºC fluids at the end of Step 2 are determined by a balance among the reduced species inherited from Step 1, the ferrous iron supplied by the low-temperature basalt alteration during Step 2, and the inputs of oxidizing species during mixing with seawater. The 20 ºC fluids produced

by reaction paths with Step 1 temperature maxima > 300 ºC and degrees of low-temperature basalt alteration <1% have high concentrations of $H_2S$ (>$10^{-4}$ M) (see square-root shaped curve in Figure 5a). Under these reaction conditions, the oxidized species supplied by seawater during mixing are the limiting reactants in the redox reactions taking place during Step 2 because of the large quantity of reduced species inherited from Step 1 including $H_2S$. In parallel, the Fe concentrations in the 20 ºC fluids are low (~$10^{-12}$ M, Figure 5b) because the high $H_2S$ concentrations maintain equilibrium with pyrite, the precipitation of which fixes Fe.

Several reaction paths produce 20 ºC fluids with extremely low $H_2S$ concentrations (<<$10^{-12}$ M) (Figure 5a). If the Step 1 temperature maximum is ≤300 ºC, a lower quantity of $H_2S$ is inherited from Step 1 such that $H_2S$ becomes one of the limiting reactants in the overall redox reactions during Step 2 (see curves dropping vertically during Step 2 in Figure 5a). The reaction paths involving a degree of low-temperature basalt alteration of 1% similarly result in extremely low $H_2S$ concentrations in the 20 ºC fluids. This is rather counterintuitive as one could expect more reduced conditions to form due to the supply of ferrous iron from the dissolution of basalt. However, the supply of Fe from low-temperature basalt alteration during mixing results in precipitation of additional pyrite, which fixes a larger amount of $H_2S$. As a result, the oxidized species supplied by seawater cease to be the limiting reactants in the redox reactions of Step 2. $H_2S$ is effectively completely oxidized at the end of mixing and $O_2$ accumulates in the fluid mixture (Figure S 10 in supplementary information). The Fe concentrations remain low (<<$10^{-12}$ M, see curves dropping vertically during Step 2 in Figure 5b) because the 20 ºC fluids reach equilibrium with goethite while the $O_2$ concentration is high (Figure S 11 in supplementary information).

Increasing the degree of low-temperature basalt alteration to 4% re-establishes relatively reduced conditions in the 20 ºC fluids yielding $H_2S$ and Fe concentrations of ca. $10^{-9}$ M and $10^{-5}$-$10^{-3}$ M, respectively (Figure 5a and b). The extra supply of Fe from low-temperature basalt alteration consumes the seawater-derived oxidized species during mixing, such that $O_2$ no longer accumulates in the fluid mixture (Figure S 10 in supplementary information) and, instead, Fe does. As a result, the 20 ºC fluids reach equilibrium with

both pyrite and goethite at the end of mixing (Figure S 4 and Figure S 11 in supplementary information). For degrees of low-temperature basalt alteration >4%, the Fe concentration in the 20 ºC fluids has no degree of freedom because of $O_2$ depletion, equilibrium with calcite which buffers the pH, and equilibrium with goethite which fixes the Fe. As a result, all reaction paths converge toward a single Fe concentration in the 20 ºC vent fluids (Figure 5b), as observed for pH, Ca, DIC and Si.

# 4. Discussion

## 4.1. Reaction conditions at Kamaʻehuakanaloa

Comparison of the measured temperature and composition of Kamaʻehuakanaloa vent fluids through time (Figure 2) suggests that the overall water-rock interactions that characterize the hydrothermal circulation have remained roughly constant for 30 years and were not substantially modified by the 1996 eruptive event over a period longer than a decade. The 20-50 ºC venting regime observed during a series of expeditions since 1987 might, thus, correspond to a chronic state that is only temporarily modified by transient volcano-tectonic events. However, our comparison gives only a broad picture of fluid evolution through time because (1) the morphology of the seafloor hosting venting was completely reshaped by the formation of Pele's Pit during the 1996 eruptive event, (2) not all expeditions sampled the same vent sites, systematically and (3) the datasets for individual samples are not always complete. This large-scale comparison, therefore, does not preclude evolution of vent fluid chemistry and temperature at smaller spatial and temporal scales. Nor do these data allow us to address what happens during the course of a volcanic eruption which, although transient, might release important chemical fluxes that could dominate the time-integrated hydrothermal output from a submarine volcano.

Sedwick et al. (1992) used $Cl^-$ depletion, alkali metal enrichment, Sr isotopes and correlations between Si and fluid temperature in 5-31ºC samples exiting the seafloor at Kamaʻehuakanaloa to infer the occurrence of high-temperature water-rock interactions at depth, as had been done previously for mid-ocean ridge 'black smokers' based on the early discoveries at the Galapagos Rift (Edmond et al., 1979). The general model of Si behavior during hydrothermal circulation is that hydrothermal fluids equilibrate with quartz at

high temperature (>300 ºC) and then rise so rapidly through the ocean crust that they neither gain nor lose Si, despite the high degree of quartz supersaturation that results from the corresponding pressure drop (Von Damm et al., 1991). However, as mentioned by Sedwick et al. (1992), the low-temperature basalt alteration required to explain the Fe enrichment in Kamaʻehuakanaloa vent fluids could also produce chemical signatures like those expected from the presence of a >300 ºC fluid endmember.

In Figure 6, the measured compositions of our Kamaʻehuakanaloa vent-fluid samples are compared to modeled compositions at the end of Step 2, where the fluid mixtures reach temperatures between 50 ºC and 20 ºC, i.e., the range of temperature measured during the 2018 SUSBEA expedition. Only the results of reaction paths involving mechanical mixing during Step 2 or a narrow degree of low-temperature basalt alteration, *F*, between 2% and 8% are shown here. Further figures showing the full range of reaction conditions considered in our work, across a broader range of *F* values, are provided in supplementary information: Figure S 12 to Figure S 20. Our model shows that while the measured Si concentrations are indeed consistent with mechanical mixing between seawater and a ≥350 ºC hydrothermal fluid endmember, the pH and alkalinity values and the concentrations of Ca, K and Fe are not. Rather, the use of multiple tracers allows us to narrow down the range of possible reaction conditions for the Kamaʻehuakanaloa vent fluids and makes it possible to distinguish between the influence of (Step 1) the maximum temperature and the rock/water ratio reached at depth and (Step 2) the degree of low-temperature basalt alteration during fluid upwelling and mixing.

Regardless of Step 1 temperature maxima, mechanical mixing is not able to explain the observed distribution of vent-fluid compositions (e.g., Figure 6, left column). Instead, the modeled Si concentrations and pH values (Figure 6a-d) only migrate towards our measured values as one increases the degree of low-temperature basalt alteration, *F*, during Step 2. For these two parameters, our 2018 data are matched most closely by models in which reaction paths involve either: (Figure 6b) Step 1 temperature maxima of 300-350 ºC and a degree of low-temperature basalt alteration of F=2% during Step 2 or (Figure 6c) Step 1 temperature maxima of ≥350 ºC and a degree of low-temperature basalt alteration of 4% during Step 2.

Increasing the degree of low-temperature basalt alteration any further only leads to a decrease of the chemical diversity and departure of the modeled fluid compositions from the measured fluid concentrations (Figure 6d and Figure S 12 in supplementary information).

However, if alkalinity is considered (Figure 6e-h), an even narrower range of possible reaction conditions is revealed. The high alkalinity values of at Kamaʻehuakanaloa compared to other submarine vent fields (Table 2) are best explained by reaction paths involving Step 1 temperature maxima of ≥350 ºC and a low-temperature basalt alteration of 4% during Step 2 whereas a F value of 2% is less consistent (Figure 6f and g, Figure S 13 in supplementary information). For the case of vent-fluid Ca and K compositions, our approach is less diagnostic: a broad range of reaction paths can account for the measured Ca and K concentrations in the 20-50 ºC vent fluids because the modeled concentrations are less sensitive to the reaction conditions than the pH values, Si concentrations or alkalinity (Figure 6i to 6p, Figure S 15 and Figure S 16 in supplementary information). For instance, reaction paths involving Step 1 temperature maxima >300 ºC and mechanical mixing during Step 2 or equilibrium mixing with a degree of low-temperature basalt alteration of 2% show some consistency with the measured Ca and K concentrations (Figure 6i, j, m and n) even though those reaction conditions are precluded by the Si and alkalinity data. In contrast, reaction paths with Step 1 temperature maxima of ≥350 ºC and a degree of low-temperature basalt alteration of 4% are required to offer consistency with all of our measured pH, Si, alkalinity and Ca concentrations (Figure 6k and o). For higher degrees of low-temperature basalt alteration, F, the diversity of Ca and K concentrations in the 20-50 ºC vent fluids decrease, as seen for Si and alkalinity, and the modeled concentrations deviate from our measured vent-fluid values (Figure 6l and p).

Unlike the case for Ca and K, consideration of Fe concentration data *does* help narrow the range of possible reaction conditions at Kamaʻehuakanaloa (Figure 6q to 6t, Figure S 17 in supplementary information). Our measured Fe concentrations are only consistent with a highly constrained set of tested reaction conditions: a Step 1 temperature maximum of ≥350 ºC and a degree of low-temperature basalt alteration of F=4% during Step 2 (Figure 6s). Reaction paths involving these same reaction conditions also

predict low $H_2$ and $H_2S$ concentrations ($<10^{-9}$M), which are consistent with those species being below our detection limits during the 2018 field program (Table 1, Figure S 10 in supplementary information). Under these same reaction conditions, the modeled sulfate, Mg and Na concentrations in 20-50 ºC vent fluids at the end of Step 2 are also consistent with measured vent-fluid values (Figure S 18, Figure S 19 and Figure S 20 in supplementary information). Note that the measurements of Mg and sulfate concentrations in Kamaʻehuakanaloa vent fluids slightly lower than seawater values suggest that any Mg and sulfate depletion produced by the formation of Mg-smectite and anhydrite during fluid upwelling is not completely overprinted by mixing with seawater in the shallow subsurface (Figure S 1 and Figure S 21).

In addition to the chemical compositions of the vent-fluid samples collected from our expedition, our model is also consistent with mineral observations in high and low-temperature basalt alteration at the seafloor and with mineral observations from Kamaʻehuakanaloa that have been reported in previous studies. As seawater percolates downward beneath the seafloor and is heated above ~150 ºC, Mg tends to be fixed into smectite and chlorite (Alt, 1995). At higher temperatures, the precipitation of epidote, amphibole, prehnite and secondary plagioclase controls Ca and Na concentrations (Alt et al., 2010). Consistent with this, our modeled Step 1 hydrothermal fluids reach equilibrium with Ca-Na-saponite, daphnite (Fe-chlorite), epidote, tremolite, prehnite and albite (Figure S 1, Figure S 9, Figure S 2, Figure S 3, Figure S 22, Figure S 23 in supplementary information).

In general, the oxidizing alteration of oceanic basalts at low-temperature in the upper portion of the volcanic section is characterized by the formation of Fe-oxyhydroxides – mostly goethite, replacing olivine – and celadonite and smectite replacing plagioclase and fixing alkalis (Alt, 1995). In extreme cases of oxidizing alteration, K-feldspar replaces plagioclase in the shallowest section of the seafloor (Alt, 1995; Santiago Ramos et al., 2020). Drilling within altered basalts of the Nintoku Seamount, which lies in the Emperor Seamount Chain, revealed a secondary mineralogy made of smectite, Fe-oxyhydroxide, iddingsite and Ca-carbonates, produced by the circulation of large quantities of cold oxidizing seawater (Révillon et al., 2007). Similarly, at Kamaʻehuakanaloa, altered basalts are characterized by extensive hydrothermal

deposits of Fe-oxyhydroxides, including goethite, and smectite ranging in composition from Fe-montmorillonite to nontronite (Malahoff et al., 1982; De Carlo et al., 1983; Emerson and Moyer, 2002; Toner et al., 2012; Rouxel et al., 2018). Recently, Ca-carbonates were also reported as ubiquitous secondary minerals at Kamaʻehuakanaloa, filling vesicles of altered basalt at vent sites (Garcia, 2019). Consistent with these observations, reaction paths involving Step 1 temperature maxima of ≥350 ºC and a degree of low-temperature basalt alteration of F=4% predict 20-50 ºC vent fluids at equilibrium with Na-Ca-Mg saponite/montmorillonite, K-feldspar, goethite, and calcite (Figure S 1, Figure S 7, Figure S 11 in supplementary information and Figure 3d). In contrast to field observations, K-fixation in our model is controlled by the precipitation of muscovite (K-Al-endmember of micas) because celadonite (ferric-mica) is absent from our database. Although nontronite is reported to occur in hydrothermal deposits at Kamaʻehuakanaloa, better consistency between modelled and observed vent-fluid composition can only be achieved when suppressing nontronite precipitation during Step 2. This suggests that either the upwelling fluid in the shallow subsurface does not precipitate nontronite at equilibrium or that the precipitation of nontronite only occurs beyond the end of Step 2, as 20-50°C vent fluids exit the seafloor. Alternatively, the thermodynamic properties of nontronite available in our database may not accurately represent those of nontronite precipitated at Kamaʻehuakanaloa.

To summarize, our modeling indicates that a temperature maximum of ≥350 ºC and a rock/water ratio of ≥1 during Step 1 together with a degree of low-temperature basalt alteration, *F*, of ~4% during fluid upwelling and mixing (Step 2) represent the reaction conditions most consistent with production of the vent-fluid compositions observed at Kamaʻehuakanaloa during our expedition. These reaction conditions represent a unifying solution that explains most of the chemical features of the Kamaʻehuakanaloa vent fluids reported here as well as mineral observations that have been reported elsewhere. The general model of simpler mechanical mixing between high temperature fluids and seawater that has previously been used to describe Si behavior during high-temperature hydrothermal circulation at mid-ocean ridges is not applicable at Kamaʻehuakanaloa because low-temperature basalt alteration during fluid upwelling and

514 mixing mobilizes Si, among other species, but can also remove it from solution through the precipitation
515 of alkalic feldspar and smectite.

516 Other mechanisms beyond our preferred model output might also exist, of course, beyond the range of
517 parameter-space that we have considered. Notably, only a limited set of temperature-rock/water ratio paths
518 during Step 1 were considered. Cool hydrothermal circulation involving very low rock/water ratios ($<5 \cdot 10^{-4}$)
519 at temperature <10 ºC (Coogan and Gillis, 2018) was not investigated, but such systems fall below the
520 range of temperatures reported for most vent-fluids exiting the summit of Kamaʻehuakanaloa (Figure 2).
521 Similarly, the effect of conductive heat loss was not investigated in our models. While our mixing model is
522 consistent with both the measured temperature and the measured concentrations of chemical species that
523 behave close to mechanical mixing during Step 2 (Mg, sulfate), this would not be the case if conductive
524 heat loss played a significant role in the temperature decrease of the fluid mixture. The relationship between
525 temperature and the degree of mixing during Step 2 is exponential such that the temperature gradient that
526 drives conductive heat loss decreases exponentially with the degree of mixing. Therefore, it seems
527 reasonable to assign most of the temperature decrease during Step 2 to mixing with seawater.

528 Like all models, the effectiveness of our model in relating it to the hydrothermal circulation at
529 Kamaʻehuakanaloa is only as good as our assumptions. However, the wide range of reaction conditions
530 considered, and the consistency of the solution presented above in accounting for the array of tracers
531 investigated reassures us of its applicability to Kamaʻehuakanaloa in its current state.

532 4.3. Kamaʻehuakanaloa as a model for low-temperature vent fluids at intraplate volcanoes?

533 In addition to the maximum temperatures and the rock/water ratios reached at depth at Kamaʻehuakanaloa
534 (Step 1), the low-temperature basalt alteration during fluid upwelling and mixing (Step 2) exerts strong
535 controls on the modeled composition of the 20-50 ºC vent fluids. On the one hand, the increase of basalt
536 alteration during Step 2 decreases the diversity of vent-fluid compositions as a function of Step 1 reaction

conditions; on the other hand, it leads to a dramatic change in the dominant reduced species in the 20-50 ºC vent fluids: an enrichment in Fe and a concurrent depletion in $H_2S$ and $H_2$.

The occurrence and extent of low-temperature basalt alteration during fluid upwelling may depend on the geometric arrangement of the steep-sloped Kamaʻehuakanaloa seamount and the associated hydrogeologic plumbing of its hydrothermal convection cell. In parallel work pursued by the SUBSEA team, oxygen and hydrogen isotopic compositions of Kamaʻehuakanaloa vent fluids were used to argue that the seawater recharging the hydrothermal system comes from Pacific Deep Waters at >3000 m, much deeper than the summit crater vents at ~1150-1300m. That study suggests that such a convection cell is made possible specifically because of the steepness of Kamaʻehuakanaloa's flanks which allow deep ocean waters to be drawn in through porous ocean crust across much shorter lateral distances from the site of discharge than would be possible across the more gently-sloping flanks of mid-ocean ridge hydrothermal systems. Simultaneously, this geometric arrangement could accommodate a much longer circulation path from the reaction zone, where maximum temperatures are reached at depth, to the summit where topography forces hydrothermal fluids to vent (Titarenko and McCaig, 2016). The magma chamber at Kamaʻehuakanaloa could be as deep as 7 km below the summit of the volcano (Duennenbier et al., 1997), significantly deeper than at mid ocean ridges. In mid-ocean ridge systems, the hydrogeological plumbing of the hydrothermal convection cell is accommodated by ridge-parallel bounding faults which allow for rapid fluid flow. This contrasts with the Kamaʻehuakanaloa seamount where the stacking of basalt flows can lead to much greater tortuosity in the up-flow path, leading to a much greater surface area of basaltic material being exposed to fluid interactions and, as a consequence, greater basalt reactivity. This combination of greater depth and tortuosity could also lead to significantly longer fluid residence times and/or flow-paths in the subsurface at Kamaʻehuakanaloa when compared to mid-ocean ridge systems. These, in turn, might be expected to give rise to the more extensive low-temperature basalt alteration that we argue for, here, as Step 2 of our conceptual model. If correct, we can hypothesize that active intraplate

seamounts should predominantly produce low-temperature Fe-rich vent fluids, as observed at Kama‘ehuakanaloa.

Intraplate hydrothermal activity across the vast interior of Earth’s Ocean basins has been disproportionately overlooked, to date, when compared to the attention paid to venting at mid-ocean ridges. Only four sites of venting on intraplate seamounts have been reported to the InterRidge vents data base across the entire Pacific (Beaulieu et al., 2013). Interestingly, two of them share characteristics with Kama‘ehuakanaloa in terms of their reported vent fluid and hydrothermal plume characteristics. In the late 1980s, low-temperature hydrothermal venting was reported at the summit of the Teahitia seamount, the most westerly active seamount of the Society Islands hotspot in the Central Pacific Ocean (Cheminee et al., 1989; Binard et al., 1992). Vent fluids were observed exiting from small Fe oxyhydroxide chimneys with fluid temperatures of ~30 ºC, pH values ranging from 5.3 to 5.6, high concentrations of Si (0.8–0.9 mmol/kg), Fe (170–190 µmol/kg) and Mn (6–13 µmol/kg) but no detectable dissolved $H_2S$ (Michard et al., 1993). More recently, German et al. (2020) measured high concentrations of total dissolvable Fe (≤186 nmol/L) and Mn (≤33 nmol/L) in the hydrothermal plume overlying the Teahitia seamount, comparable to hydrothermal plume values measured at Kama‘ehuakanaloa (Sakai et al., 1987; Bennett et al., 2011).

At the Vailulu’u seamount, an active submarine volcano located 45 km east of the easternmost island in the Samoan archipelago, Staudigel et al. (2006) reported low-temperature vents (<81 ºC) exiting from centimeter-to-meter-sized Fe-oxide chimneys together with evidence of high concentrations of dissolved $CO_2$. As at Kama‘ehuakanaloa, the Teahitia and Vailulu’u seamounts stand >1500m above the surrounding seafloor. The similarity between the Kama‘ehuakanaloa, Teahitia and Vailulu’u seamounts suggests that chronic hydrothermal activity associated with submarine intraplate hotspot volcanoes may predominantly lead to low-temperature vent fluids enriched in Fe, Mn, Si, $CO_2$ compared to seawater and depleted in $H_2$ and $H_2S$ compared to mid-ocean ridge ‘black smokers’.

It has long been known that hydrothermal activity can inject detectable amounts of He enriched in $^3He$ into the oceans from submarine venting, from both mid-ocean ridges and intraplate volcanoes (Lupton et

al., 1977; Lupton, 1998). Recent work from the US GEOTRACES program has shown that important fluxes of Fe can also be injected along with that venting which can be upwelled to the surface ocean (Resing et al., 2015). However, while the principal source for Fe at mid-ocean ridges is considered to be from low-temperature venting with Fe concentrations in the 10-100 µM range (German et al., 2015), the Fe concentrations of vent fluids at intraplate systems like Kamaʻehuakanaloa are 1-2 orders of magnitude higher and are injected into the ocean at much shallower depths beneath the photic zone (Jenkins et al., 2020). Therefore, Fe fluxes associated with intraplate volcanoes may be disproportionately important in terms of global biogeochemical cycles, beyond the deep, dark seafloor.

## 5. Conclusions

New data on submarine vent-fluid compositions acquired at the Kamaʻehuakanaloa seamount during the SUBSEA exploration aboard the *E/V Nautilus* in 2018, coupled with a 30-year record of Kamaʻehuakanaloa fluid composition data, were used to develop geochemical models of water-rock-gas reactions that produce low-temperature vent fluids at intraplate submarine volcanoes. Our model indicates that the compositions of 20-50 ºC vent fluids at Kamaʻehuakanaloa, which are enriched in Fe, Si and $CO_2$ and depleted in $H_2S$, are not consistent with a simple model of mechanical mixing between seawater and high-temperature vent-fluid. Instead, they appear to reflect an additional stage of subsurface equilibrium mixing between a ≥350 ºC hydrothermal fluid end-member and seawater (Step 1), followed by low-temperature chemical alteration of basalt (Step 2) as the resultant hot fluid mixture rises toward the overlying seafloor. Despite the low proportion of additional basalt involved at Step 2 of this process (i.e., only ~4% of the amount of basalt involved in the initial high-temperature reactions at depth), this late reaction step has dramatic impacts on the compositions of the 20-50 ºC vent fluids that are emitted into the ocean, decreasing their Si and $H^+$ concentrations compared to mechanical mixing and determining which of $Fe^{2+}$ or $H_2S+H_2$ is the dominant reduced species released from the seafloor. We hypothesize that it is the low-temperature basalt alteration during Step 2 fluid upwelling that gives the Kamaʻehuakanaloa vent fluids their distinctive composition and that this process, in turn, may arise directly from Kamaʻehuakanaloa's seamount topography.

Specifically, the very steepness of the seamount's flanks could accommodate recharge at great depths where the high-temperature reaction zone could be located, resulting in a much longer circulation pathway from there to the (potentially thousands of meters shallower) summit where the vent-fluids are emitted. Thus, while the recharge path at Kamaʻehuakanaloa may be shorter than for submarine vents at Mid-Ocean Ridges, the up-flow path prior to exit at the seafloor may be significantly longer. Such a circulation geometry could provide an opportunity for extensive low-temperature chemical alteration of basalt via a mechanism that should not be expected at mid-ocean ridges where recharge and discharge are predicted to occur along axis from one another. By contrast, the work we present here could be representative of processes at several other active intraplate seamounts which, as recently shown for Kamaʻehuakanaloa, could contribute substantially to the global Fe-ocean cycle. Such systems could produce low-temperature venting with Fe concentrations 1-2 orders of magnitude higher than at mid-ocean ridges which they would discharge at much shallower depths, injecting this essential micro-nutrient into the oceans closer to the sunlit upper ocean where it can regulate $CO_2$ draw down by stimulating primary productivity.

## 6. Research data

The output files of the EQ3/6 reaction path calculation can be found in a Mendeley data repository at the following address: https://data.mendeley.com/datasets/n6rbd534h3/1

## 7. Appendix A. Supplementary Material

A supplementary file associated with this paper contains one additional table and 23 figures:

- the chemical composition of the basalt used in the modeling
- the saturation indexes for saponite, epidote, tremolite, pyrite, muscovite, quartz, K-feldspar, daphnite, goethite, anhydrite, prehnite, albite as functions of temperature during modeled reaction pathways
- Na, Cl, $O_2$ and $H_2$ concentrations as functions of temperature during modeled reaction pathways

- the Si, alkalinity, DIC, Ca, K, Fe, sulfate, Mg and Na concentrations as functions of pH values for modeled and measured 20-50 ºC vent fluids

## ACKNOWLEDGMENTS

This work was supported by NASA Planetary Science and Technology Through Analog Research (PSTAR) Program (NNH16ZDA001N-PSTAR) grant (16-PSTAR16_2–0011) to Dr D. S. S. Lim, NOAA Office of Ocean Exploration and Research, Ocean Exploration Trust, NOAA-OER grant NA17OAR0110336, NASA Postdoctoral Fellowship and L'Oréal USA For Women in Science Fellowship to E.T.R. This research used samples and data provided by the Ocean Exploration Trust's Nautilus Exploration Program, Cruise NA100. We thank the cruise expedition Leader N. Raineault, the ROV Hercules/Argus team and the crew of the E/V Nautilus for their assistance while at sea. We are grateful to all members of the SUBSEA team and to the team of the Inner Space Center at the University of Rhode Island Graduate School of Oceanography who made this study possible: John A. Breier, Eric Chan, Josh Chernov, Tamar Cohen, Matthew Deans, Angela Garcia, Michelle Hauer, Renato Kane, Shannon Kobs Nawotniak, David Lees, Justin Lowe, Leigh Marsh, Matthew J. Miller, Miles Saunders, Khaled Sharif, Ashley Shields. We thank the reviewers and the associate editor for helpful and insightful reviews. This is SUBSEA Publication Number: SUBSEA-2018-002.

651 REFERENCES


652 Alt J. C. (1995) Subseafloor processes in mid-ocean ridge hydrothermal systems. Washington DC, AGU Geophys.
653 Monogr. Ser. 91, 85-114.

654 Alt J. C., Laverne C., Coggon R. M., Teagle D. A. H., Banerjee N. R., Morgan S., Smith-Duque C. E., Harris M. and
655 Galli L. (2010) Subsurface structure of a submarine hydrothermal system in ocean crust formed at the East Pacific
656 Rise, ODP/IODP Site 1256. Geochem. Geophys. Geosyst. 11.

657 Arvidson R. S. (1999) The dolomite problem: control of precipitation kinetics by temperature and saturation state.
658 Am. J. Sci. 299, 257–288.

659 Aubaud C. (2004) Hydrogen partition coefficients between nominally anhydrous minerals and basaltic melts.
660 Geophys. Res. Lett. 31, L20611.

661 Beaulieu S. E., Baker E. T. and German C. R. (2015) Where are the undiscovered hydrothermal vents on oceanic
662 spreading ridges? Deep Sea Research Part II: Topical Studies in Oceanography 121, 202–212.

663 Beaulieu S. E., Baker E. T., German C. R. and Maffei A. (2013) An authoritative global database for active
664 submarine hydrothermal vent fields. Geochem. Geophys. Geosyst. 14, 4892–4905.

665 Bennett S. A., Hansman R. L., Sessions A. L., Nakamura K. and Edwards K. J. (2011) Tracing iron-fueled microbial
666 carbon production within the hydrothermal plume at the Lō‘ihi seamount. Geochim. Cosmochim. Ac. 75, 5526–
667 5539.

668 Binard N., Hékinian R., Cheminée J. L. and Stoffers P. (1992) Styles of eruptive activity on intraplate volcanoes in
669 the Society and Austral hot spot regions: bathymetry, petrology, and submersible observations. J. Geophys. Res. 97,
670 13999.

671 Bischoff J. L. and Rosenbauer R. J. (1985) An empirical equation of state for hydrothermal seawater (3.2% NaCl).
672 Am. J. Sci. 285, 725–763.

673 Bowers T. S. and Taylor H. P. (1985) An integrated chemical and stable-isotope model of the origin of Midocean
674 Ridge Hot Spring Systems. J. Geophys. Res. 90, 12583.

675 Bradley A. S. and Summons R. E. (2010) Multiple origins of methane at the Lost City hydrothermal field. Earth
676 Planet. Sc. Lett. 297, 34–41.

677 Bruland K. W. and Lohan M. C. (2006) Controls of trace metals in seawater. The oceans and marine geochemistry
678 6, 23–47.

679 Cartigny P., Pineau F., Aubaud C. and Javoy M. (2008) Towards a consistent mantle carbon flux estimate: Insights
680 from volatile systematics ($H_2O$/Ce, δD, $CO_2$/Nb) in the North Atlantic mantle (14° N and 34° N). Earth Planet. Sc.
681 Lett. 265, 672–685.

682 Cheminee J. L., Hekinian R., Talandier J., Albarede F., Devey C. W., Francheteau J. and Lancelot Y. (1989)
683 Geology of an active hot spot: Teahitia-Mehetia region in the South Central Pacific. Mar. Geophys. Res. 11, 27–50.

684 Cline J. D. (1969) Spectrometric determinationof hydrogen sulfide in natural waters. Limnol. Oceanogr. 14, 454–
685 458.

686 Coogan L. A. and Gillis K. M. (2018) Low-temperature alteration of the seafloor: impacts on ocean chemistry.
687 Annu. Rev. Earth Planet. Sci. 46, 21–45.

688 Davis A. S. and Clague D. A. (1998) Changes in the hydrothermal system at Lō‘ihi Seamount after the formation of
689 Pele’s pit in 1996. Geology 26, 399–402.

De Carlo E. H., McMurtry G. M. and Yeh H.-W. (1983) Geochemistry of hydrothermal deposits from Lō‘ihi submarine volcano, Hawaii. Earth Planet. Sc. Lett. 66, 438–449.

Dick G. J. (2019) The microbiomes of deep-sea hydrothermal vents: distributed globally, shaped locally. Nat. Rev. Microbiol. 17, 271–283.

Dixon J. E. and Clague D. A. (2001) Volatiles in basaltic glasses from Lō‘ihi Seamount, Hawaii: Evidence for a relatively dry plume component. J. Petrol. 42, 627–654.

Duennenbier F. K., Becker N. C. and Caplan-Auerbach, Jacqueline; Clague, D. A.; Cowen, J.; Cremer, M.; Garcia, M.; Goff, F.; Malahoff, A.; McMurtry, G. M.; Midson, B. P.; Moyer, Craig L.; Norman, N.; Okubo, P.; Resing, J. A.; Rhodes, J. M.; Rubin, K.; Sansone, F. J.; Smith, J. R.; Spencer, K.; Wen, X.; and Wheat, C. G. (1997) Researchers rapidly respond to submarine activity at Lō‘ihi Volcano, Hawaii. Eos Trans. AGU 78, 229.

Edmond J. M., Measures C., McDuff R. E., Chan L. H., Collier R., Grant B., Gordon L. I. and Corliss J. B. (1979) Ridge crest hydrothermal activity and the balances of the major and minor elements in the ocean: The Galapagos data. Earth Planet. Sc. Lett. 46, 1–18.

Ely T. (2020) Thermodynamic cartography in basalt-hosted hydrothermal systems. Doctoral dissertation, Arizona State University.

Emerson D. and Moyer C. L. (2002) Neutrophilic Fe-oxidizing bacteria are abundant at the Lō‘ihi seamount hydrothermal vents and play a major role in Fe oxide deposition. AEM 68, 3085–3093.

Gamo T., Ishibashi J.-I., Sakai H. and Tilbrook B. (1987) Methane anomalies in seawater above the Lō‘ihi submarine summit area, Hawaii. Geochim. Cosmochim. Ac. 51, 2857–2864.

Garcia A. (2019) Habitability potential of Enceladus: an analog study of the Lō‘ihi seamount system in Hawai’i. Master thesis, Idaho State University.

Garrels R. M. and Thompson M. E. (1962) A chemical model for sea water at 25° C and one atmosphere total pressure. Am. J. Sci. 260, 57–66.

German C. R., Casciotti K. A., Dutay J.-C., Heimbürger L.-E., Jenkins W. J., Measures C. I., Mills R. A., Obata H., Schlitzer R. and Tagliabue A. (2016) Hydrothermal impacts on trace element and isotope ocean biogeochemistry. Philos. T. R. Soc. A. 374, 20160035.

German C. R., Legendre L. L., Sander S. G., Niquil N., Luther G. W., Bharati L., Han X. and Le Bris N. (2015) Hydrothermal Fe cycling and deep ocean organic carbon scavenging: Model-based evidence for significant POC supply to seafloor sediments. Earth Planet. Sc. Lett. 419, 143–153.

German C. R., Resing J. A., Xu G., Yeo I. A., Walker S. L., Devey C. W., Moffett J. W., Cutter G. A., Hyvernaud O. and Reymond D. (2020) Hydrothermal activity and seismicity at Teahitia Seamount: reactivation of the society islands hotspot? Front. Mar. Sci. 7, 73.

German C. R. and Seyfried W. E. (2014) Hydrothermal processes. In Treatise on geochemistry 8, 191–233.

German C. R. and Von Damm K. L. (2006) Hydrothermal processes. In Treatise on geochemistry 6, 181–222.

Glazer B. T. and Rouxel O. J. (2009) Redox speciation and distribution within diverse iron-dominated microbial habitats at Lō‘ihi Seamount. Geomicrobiol. J. 26, 606–622.

Grozeva N. G., Klein F., Seewald J. S. and Sylva S. P. (2020) Chemical and isotopic analyses of hydrocarbon-bearing fluid inclusions in olivine-rich rocks. Philos. T. R. Soc. A. 378, 20180431.

Helgeson H. C. (1969) Thermodynamics of hydrothermal systems at elevated temperatures and pressures. Am. J. Sci. 267, 729–804.

730 Helgeson H. C., Delany J. M., Nesbitt N. W. and Bird D. K. (1978) Summary and critique of the thermodynamic
731 properties of rock-forming minerals. Am. J. Sci. 278.

732 Hilton D. R., McMurtry G. M. and Goff F. (1998) Large variations in vent fluid $CO_2/^3He$ ratios signal rapid changes
733 in magma chemistry at Lō‘ihi seamount, Hawaii. Nature 396, 359–362.

734 Jannasch H. W. and Mottl M. J. (1985) Geomicrobiology of deep-sea hydrothermal vents. Science 229, 717–725.

735 Jenkins W. J., Hatta M., Fitzsimmons J. N., Schlitzer R., Lanning N. T., Shiller A., Buckley N. R., German C. R.,
736 Lott III D. E. and Weiss G. (2020) An intermediate-depth source of hydrothermal 3He and dissolved iron in the
737 North Pacific. Earth Planet. Sc. Lett. 539, 116223.

738 Karl D. M., McMurtry G. M., Malahoff A. and Garcia M. O. (1988) Lō‘ihi seamount, Hawaii: a mid-plate volcano
739 with a distinctive hydrothermal system. Nature 335, 532–535.

740 Klein F., Grozeva N. G. and Seewald J. S. (2019) Abiotic methane synthesis and serpentinization in olivine-hosted
741 fluid inclusions. Proc. Natl. Acad. Sci. USA 116, 17666–17672.

742 Lim D. S. S., Raineault N. A., Alanis B., Brier J. A., Chan E., Emerson D., Garcia A., German C. R., Huber J. A.,
743 Kobs Nawotniak S., Milesi V., Shields A., Shock E., Smith A., Seewald J. S., Trembath-Reichert E., Mirmalek Z.,
744 Miller M. J., Cohen T., Lees D. and Deans M. (2019) SUBSEA 2018 Expedition to the Lō‘ihi Seamount, Hawai‘i
745 (New Frontiers in Ocean Exploration: The E/V Nautilus, NOAA Ship Okeanos Explorer, and R/V Falkor 2018 Field
746 Season) eds. N. A. Raineault and J. Flanders. Oceanog. 32, 48–49.

747 Lupton J. (1998) Hydrothermal helium plumes in the Pacific Ocean. J. Geophys. Res. 103, 15853–15868.

748 Lupton J. E., Weiss R. F. and Craig H. (1977) Mantle helium in hydrothermal plumes in the Galapagos Rift. Nature
749 267, 603–604.

750 Malahoff A., McMurtry G. M., Wiltshire J. C. and Yeh H.-W. (1982) Geology and chemistry of hydrothermal
751 deposits from active submarine volcano Lō‘ihi, Hawaii. Nature 298, 234–239.

752 Martin W., Baross J., Kelley D. and Russell M. J. (2008) Hydrothermal vents and the origin of life. Nat. Rev.0
753 Microbiol. 6, 805–814.

754 McCollom T. M. and Shock E. L. (1997) Geochemical constraints on chemolithoautotrophic metabolism by
755 microorganisms in seafloor hydrothermal systems. Geochim. Cosmochim. Ac. 61, 4375–4391.

756 McDermott J. M., Seewald J. S., German C. R. and Sylva S. P. (2015) Pathways for abiotic organic synthesis at
757 submarine hydrothermal fields. Proc. Natl. Acad. Sci. USA 112, 7668–7672.

758 McDermott J. M., Sylva S. P., Ono S., German C. R. and Seewald J. S. (2020) Abiotic redox reactions in
759 hydrothermal mixing zones: Decreased energy availability for the subsurface biosphere. Proc. Natl. Acad. Sci. USA
760 117, 20453–20461.

761 Michael P. J. (1988) The concentration, behavior and storage of $H_2O$ in the suboceanic upper mantle: Implications
762 for mantle metasomatism. Geochim. Cosmochim. Ac. 52, 555–566.

763 Michard A., Michard G., Stüben D., Stoffers P., Cheminée J.-L. and Binard N. (1993) Submarine thermal springs
764 associated with young volcanoes: The Teahitia vents, Society Islands, Pacific Ocean. Geochim. Cosmochim. Ac. 57,
765 4977–4986.

766 Milesi V., Shock E., Ely T., Lubetkin M., Sylva S. P., Huber J. A., Smith A. R., Nawotniak S. K., Mirmalek Z. and
767 German C. R. (2021) Forward geochemical modeling as a guiding tool during exploration of Sea Cliff hydrothermal
768 field, Gorda Ridge. Planet. Space Sci. 197, 105151.

769 Moore J. G., Clague D. A. and Normark W. R. (1982) Diverse basalt types from Lō‘ihi seamount, Hawaii. Geology
770 10, 88–92.

Mottl M. J., Seewald J. S., Wheat C. G., Tivey M. K., Michael P. J., Proskurowski G., McCollom T. M., Reeves E., Sharkey J., You C.-F., Chan L.-H. and Pichler T. (2011) Chemistry of hot springs along the Eastern Lau Spreading Center. Geochim. Cosmochim. Ac. 75, 1013–1038.

Reed M. and Spycher N. (1984) Calculation of pH and mineral equilibria in hydrothermal waters with application to geothermometry and studies of boiling and dilution. Geochim. Cosmochim. Ac. 48, 1479–1492.

Resing J. A., Sedwick P. N., German C. R., Jenkins W. J., Moffett J. W., Sohst B. M. and Tagliabue A. (2015) Basin-scale transport of hydrothermal dissolved metals across the South Pacific Ocean. Nature 523, 200–203.

Révillon S., Teagle D. A. H., Boulvais P., Shafer J. and Neal C. R. (2007) Geochemical fluxes related to alteration of a subaerially exposed seamount: Nintoku seamount, ODP Leg 197, Site 1205. Geochem. Geophys. Geosyst. 8, n/a-n/a.

Rimstidt J. D. and Barnes H. L. (1980) The kinetics of silica-water reactions. Geochim. Cosmochim. Ac. 44, 1683–1699.

Rosenthal A., Hauri E. H. and Hirschmann M. M. (2015) Experimental determination of C, F, and H partitioning between mantle minerals and carbonated basalt, $CO_2$/Ba and $CO_2$/Nb systematics of partial melting, and the $CO_2$ contents of basaltic source regions. Earth Planet. Sc. Lett. 412, 77–87.

Rouxel O., Toner B., Germain Y. and Glazer B. (2018) Geochemical and iron isotopic insights into hydrothermal iron oxyhydroxide deposit formation at Lō‘ihi Seamount. Geochim. Cosmochim. Ac. 220, 449–482.

Saal A. E., Hauri E. H., Langmuir C. H. and Perfit M. R. (2002) Vapour undersaturation in primitive mid-ocean-ridge basalt and the volatile content of Earth’s upper mantle. Nature 419, 451–455.

Sakai H., Tsubota H., Nakai T., Ishibashi J., Akagi T., Gamo T., Tilbrook B., Igarashi G., Kodera M., Shitashima K., Nakamura S., Fujioka K., Watanabe M., McMurty G., Malahoff A. and Ozima M. (1987) Hydrothermal activity on the summit of Lō‘ihi Seamount, Hawaii. Geochem. J. 21, 11–21.

Santiago Ramos D. P., Coogan L. A., Murphy J. G. and Higgins J. A. (2020) Low-temperature oceanic crust alteration and the isotopic budgets of potassium and magnesium in seawater. Earth Planet. Sc. Lett. 541, 116290.

Sedwick P. N., McMurtry G. M., Hilton D. R. and Goff F. (1994) Carbon dioxide and helium in hydrothermal fluids from Lō‘ihi Seamount, Hawaii, USA: Temporal variability and implications for the release of mantle volatiles. Geochim. Cosmochim. Ac. 58, 1219–1227.

Sedwick P. N., McMurtry G. M. and Macdougall J. D. (1992) Chemistry of hydrothermal solutions from Pele’s Vents, Lō‘ihi Seamount, Hawaii. Geochim. Cosmochim. Ac. 56, 3643–3667.

Seewald J. S., Doherty K. W., Hammar T. R. and Liberatore S. P. (2002) A new gas-tight isobaric sampler for hydrothermal fluids. Deep Sea Research Part I: Oceanographic Research Papers 49, 189–196.

Shock E. L. and Helgeson H. C. (1988) Calculation of the thermodynamic and transport properties of aqueous species at high pressures and temperatures: Correlation algorithms for ionic species and equation of state predictions to 5 kb and 1000°C. Geochim. Cosmochim. Ac. 52, 2009–2036.

Shock E. L., Helgeson H. C. and Sverjensky D. A. (1989) Calculation of the thermodynamic and transport properties of aqueous species at high pressures and temperatures: Standard partial molal properties of inorganic neutral species. Geochim. Cosmochim. Ac. 53, 2157–2183.

Shock E. L., Oelkers E. H., Johnson J. W., Sverjensky D. A. and Helgeson H. C. (1992) Calculation of the thermodynamic properties of aqueous species at high pressures and temperatures. Effective electrostatic radii, dissociation constants and standard partial molal properties to 1000°C and 5 kbar. J. Chem. Soc., Faraday Trans. 88, 803–826.

812 Shock E. L., Sassani D. C., Willis M. and Sverjensky D. A. (1997) Inorganic species in geologic fluids: Correlations
813 among standard molal thermodynamic properties of aqueous ions and hydroxide complexes. Geochim. Cosmochim.
814 Ac. 61, 907–950.

815 Staudigel H., Hart S. R., Pile A., Bailey B. E., Baker E. T., Brooke S., Connelly D. P., Haucke L., German C. R.,
816 Hudson I., Jones D., Koppers A. A. P., Konter J., Lee R., Pietsch T. W., Tebo B. M., Templeton A. S., Zierenberg
817 R. and Young C. M. (2006) Vailulu'u Seamount, Samoa: Life and death on an active submarine volcano. Proc. Natl.
818 Acad. Sci. USA 103, 6448–6453.

819 Sverjensky D. A., Shock E. L. and Helgeson H. C. (1997) Prediction of the thermodynamic properties of aqueous
820 metal complexes to 1000°C and 5 kb. Geochim. Cosmochim. Ac. 61, 1359–1412.

821 Titarenko S. S. and McCaig A. M. (2016) Modelling the Lost City hydrothermal field: influence of topography and
822 permeability structure. Geofluids 16, 314–328.

823 Toner B. M., Berquó T. S., Michel F. M., Sorensen J. V., Templeton A. S. and Edwards K. J. (2012) Mineralogy of
824 iron microbial mats from Lō'ihi Seamount. Front. Microbio. 3.

825 Von Damm K. L., Bischoff J. L. and Rosenbauer R. J. (1991) Quartz solubility in hydrothermal seawater; an
826 experimental study and equation describing quartz solubility for up to 0.5 M NaCl solutions. Am. J. Sci. 291, 977–
827 1007.

828 Von Damm K. L., Edmond J. M., Grant B., Measures C. I., Walden B. and Weiss R. F. (1985) Chemistry of
829 submarine hydrothermal solutions at 21 °N, East Pacific Rise. Geochim. Cosmochim. Ac. 49, 2197–2220.

830 Welhan J. A. (1988) Origins of methane in hydrothermal systems. Chem. Geol. 71, 183–198.

831 Wheat C. G., Jannasch H. W., Plant J. N., Moyer C. L., Sansone F. J. and McMurtry G. M. (2000) Continuous
832 sampling of hydrothermal fluids from Lō'ihi Seamount after the 1996 event. J. Geophys. Res. 105, 19353–19367.

833 Wheat C. G. and Mottl M. J. (2000) Composition of pore and spring waters from Baby Bare: global implications of
834 geochemical fluxes from a ridge flank hydrothermal system. Geochim. Cosmochim. Ac. 64, 629–642.

835 Wolery T. J. (2010) EQ3/6 A Software Package for Geochemical Modeling., Lawrence Livermore National
836 Lab.(LLNL), Livermore, CA (United States).

837 Wolery T. J. and Jove-Colon C. (2004) Qualification of thermodynamic data for geochemical modeling of mineral-
838 water interactions in dilute systems (Yucca Mountain Project, Las Vegas, Nevada). No. ANL-WIS-GS-000003 REV
839 00.

840

841 Kama'ehuakanaloa

*Table 1. Locations and chemical compositions of fluid samples collected during the 2018 SUBSEA expedition*

| Sample (NA100-) | 002 | 001 | 039 | 040 | 019 | 054 | 053 | 061 | 060 | 080 | 079 | 059 |
|---|---|---|---|---|---|---|---|---|---|---|---|---|
| Marker* | 34 | 34 | 38 | 38 | 31[g] | 2 | 2 | 57 | 57 | 57' | 57' | Bottom seawater |
| Site* (lat; long; depth (m)) | Spillway Area (18.906; -155.257; 1270±3) | | | | | Lohiau area (18.909; -155.257; 1179±2) | | Pohaku (18.901; -155.258; 1184±2) | | | | |
| Temperature max. (ºC)[a] | 41 | 41 | 39 | 37 | 31 | 22 | 21 | 15 | 18 | 21 | 21 | - |
| pH (25 ºC) | 5.8 | 6.0 | 6.0 | 6.1 | 6.0 | 6.2 | 6.2 | 5.4 | 5.7 | 5.7 | 5.7 | 7.4 |
| Alkalinity[b] (meq/kg) | 14.3 | 14.3 | 13.5 | 9.2 | 8.4 | 8.8 | 8.9 | 6.5 | 11.6 | 13.6 | 12.9 | 2.3 |
| Na (mmol/kg) | 459 | 463 | 464 | 460 | 462 | 490 | 464 | 465 | 463 | 466 | 464 | - |
| Cl[b] (mmol/kg) | - | 545 | 545 | 542 | 544 | 541 | 543 | 540 | 538 | 537 | 538 | 539 |
| Mg (mmol/kg) | 51.5 | 51.5 | 52.0 | 52.2 | 50.0 | 52.5 | 52.8 | 54.0 | 55.0 | 54.7 | 54.5 | - |
| Ca[b] (mmol/kg) | 15.1 | 15.8 | 15.3 | 14.3 | 14.9 | 16.0 | 16.3 | 10.9 | 11.3 | 11.4 | 10.6 | 10.3 |
| K (mmol/kg) | 12.2 | - | 12.1 | 11.3 | 12.4 | 16.6 | 11.4 | 10.7 | 11.1 | 11.7 | 11.7 | - |
| Sulfate (mmol/kg)[c] | 27.0 | 26.7 | 26.9 | 27.3 | 25.8 | 27.0 | 27.0 | 27.9 | 27.3 | 26.6 | 26.8 | 28.2 |
| Si (mmol/kg) | 2.8 | 2.7 | 2.7 | 1.5 | 1.9 | 1.7 | 1.5 | 0.6 | 1.4 | 1.8 | 1.9 | - |
| Fe (µmol/kg) | 413 | 517 | 579 | 289 | 384 | 369 | 285 | 308 | 758 | 980 | 978 | 0 |
| Mn (µmol/kg) | 40 | 40 | 38 | 24 | 25 | 73 | 45 | 10 | 18 | 21 | 22 | - |
| Al (µmol/kg) | n.d. | n.d. | n.d. | n.d. | n.d. | n.d. | n.d. | n.d. | n.d. | n.d. | n.d. | - |
| Sr (µmol/kg) | 104 | 103 | 103 | 95 | 98 | - | 102 | 87 | 88 | 87 | 87 | - |
| Ba (µmol/kg) | 0.7 | 0.7 | 0.9 | 0.7 | 0.9 | - | 0.7 | 0.7 | 1.0 | 0.6 | 1.0 | - |
| B (µmol/kg) | 398 | 402 | 424 | 410 | 398 | 553 | 388 | 424 | 452 | 491 | 484 | - |
| Li (µmol/kg) | 53 | 53 | 52 | 42 | 44 | 76 | 40 | 32 | 38 | 45 | 45 | - |
| Rb (µmol/kg) | 5.0 | 4.9 | 4.7 | 3.3 | 4.6 | 5.8 | 3.5 | 2.0 | 2.8 | 3.4 | 3.4 | - |
| Cs (µmol/kg) | 0.24 | 0.24 | 0.26 | 0.23 | 0.26 | 0.48 | 0.24 | 0.24 | 0.24 | 0.24 | 0.25 | - |
| Cu (µmol/kg) | 0.9 | 1.1 | 1.4 | 5.3 | 1.6 | 6.4 | 0.5 | 1.6 | 1.3 | 0.9 | 1.8 | - |
| Zn (µmol/kg) | 27.6 | 27.9 | 7.7 | 6.0 | 32.5 | 134.4 | 12.4 | 22.9 | 4.3 | 4.0 | 14.2 | - |
| $H_2$ (µmol/kg)[d] | <3 | <3 | <3 | <3 | <3 | <3 | <3 | <3 | <3 | <3 | <3 | - |
| $CO_2$ (mmol/kg)[d] | 31.2 | 31.2 | 30.0 | 18.3 | 17.4 | 14.2 | 14.0 | 43.8 | 94.1 | 124.3 | 125.8 | - |
| $CH_4$ (µmol/kg)[e] | 1.5 | 1.3 | 1.2 | 0.8 | 1.4 | 0.6 | 0.6 | 1.6 | 2.8 | 4.3 | 3.8 | - |
| $H_2S$ (µmol/kg)[f] | <1 | <1 | <1 | <1 | <1 | <1 | <1 | <1 | <1 | <1 | <1 | - |

*Marker and site from Rouxel et al. (2018)

[a]Temperature maximum recorded during the IGT sampling

Analysis with ICP-MS, unless otherwise noted: [b]Gran titration, [c]ion chromatography, [d]GC-TCD, [e]GC-FID, [f]spectrophotometry Cline (1969)

[g]Duplicate sample leaked

n.d. = not detected

Estimated uncertainties ($2\sigma$) are as follow: pH (25ºC) values ±0.1 unit; Na, Mg, Cl, Ca, K, sulfate concentrations ±3%; $SiO_2$, Fe, Mn, Sr, Ba, Li, Rb, Cs, Cu, Zn concentrations ±5%; $CH_4$ and $CO_2$ concentrations ±10% and ±5%, respectively.

*Table 1. Vent-fluid compositions from Lō'ihi compared with submarine vent fields from various other geologic settings*

| Vent field | Seawater | Lō'ihi [a] | 21ºN, EPR [b] | Mariner | Baby Bare (Spring water) |
|---|---|---|---|---|---|
| Geologic setting | - | Intraplate volcano | Mid ocean ridge | Back arc | Ridge flank |
| Max. T (ºC) | 2 | 41 | 350 | 363 | 25 |
| pH (25 ºC) | 7.8 | 5.9 | 3.4 | 2.7 | 8.3 |
| Alk. (meq/kg) | 2.3 | 14.3 | -0.4 | -2.25 | 0.43 |
| Cl (mmol/kg) | 546 | 546 | 489 | 605 | 554 |
| $SO_4$ (mmol/kg) | 28 | 26.9 | 0.5 | - | 17.8 |
| Na (mmol/kg) | 468 | 460.8 | 432 | 439 | 473 |
| K (mmol/kg) | 10.2 | 12.4 | 23 | 36.9 | 6.9 |
| Ca (mmol/kg) | 10.3 | 15.5 | 16 | 43.8 | 55.2 |
| Mg (mmol/kg) | 53 | 51.5 | 0 | 1.9 | 0.98 |
| Si (mmol/kg) | 0.1 | 2.8 | 18 | 15.1 | 0.4 |
| Fe (µmol/kg) | <0.001 | 465 | 1,664 | 12991 | <0.1 |
| Mn (µmol/kg) | <0.001 | 40 | 960 | 5723 | 7.8 |
| $CH_4$ (µmol/kg) | - | 1.4 | 70 | - | - |
| $H_2$ (mmol/kg) | - | b.d.l | 1.7 | - | - |
| $CO_2$ (mmol/kg) | - | 31.2 | 5.7 | 39.8 | 0.4 |
| $H_2S$ (mmol/kg) | - | b.d.l | 7.3 | 9.3 | - |

[a] Average values of the 2018 SUBSEA fluids sampled at Marker 34.
[b] Measured composition of vent fluids are corrected for entrainment of seawater during sampling based on the quantitative removal of Mg from the fluid during water-rock reactions.
Data are from Bruland et al. (2006) for seawater, Humphris and Klein (2017) for 21ºN EPR and Mariner vent fields (original data from Von Damm et al. (1985) and Mottl et al. (2011), respectively), Wheat and Mottl (2000) for Baby Bare.
Abbreviation: Max. T = maximum temperature; Alk. = Alkalinity; - = not determined; b.d.l = below detection limit.

Figure 1. (a) Conceptual model of hydrothermal circulation producing low-temperature vent fluids at Kamaʻehuakanaloa. In Step 1, seawater reacts progressively with basalt and volcanic gases ($CO_2$, $SO_2$ and $H_2O$) in an open system along an increase of temperature from 2 ºC to a temperature maximum that ranges between 50 ºC and 400 ºC, and a corresponding increase of rock/water ratio from 0.1 to 1.1. In Step 2, the hydrothermal fluid produced during Step 1 mixes with 2 ºC seawater in an open system in which it also continues to react with basalt until the fluid mixture reaches 20 ºC. The proportion of basalt and gas reacting during Step 2 is modelled as a fraction, F=0% to F=20%, of the amount of basalt reacting during Step 1. Both mechanical and equilibrium mixing were considered during Step 2. (b) Rock/water weight ratios during Step 1 (black line) and Step 2 (colored lines) are shown as functions of the maximum model temperatures reached during Step 1.

Figure 2. Evolution of Kamaʻehuakanaloa vent fluid compositions and temperatures through time. The blue, orange, white and red boxes represent the periods of pre-eruption, 1988-1993 (Karl et al., 1988; Sedwick et al., 1992, 1994; Hilton et al., 1998), syn-eruption, 1996-1997 (Hilton et al., 1998; Wheat et al., 2000), post-eruption, 2006-2008 (Glazer and Rouxel, 2009; Rouxel et al., 2018) and our SUBSEA data (2018; this study). The numbering above each box indicates the number of measurements for each species within each dataset. Note that no data are available for Na, Cl and DIC concentrations from Glazer and Rouxel (2009) and Rouxel et al. (2018) and that the estimations of DIC concentrations from Karl et al. (1988) and Sedwick et al. (1992) were excluded. The samples considered are from Pele's vents for the pre-eruption period and from Pele's Pit (Spillway, Lohiau and Hiolo areas) and the Pohaku area for the post-eruption period. Alk. stands for alkalinity and T (ºC) for temperature.

Figure 3. pH values, Ca concentrations, DIC concentrations and calcite saturation indexes as functions of temperature during modeled reaction pathways at Kamaʻehuakanaloa. Seawater composition is shown with an open star and the solid black line represents Step 1 fluid compositions. The color gradation from purple to red represents families of paths for Step 2 fluid compositions originating with

Step 1 fluid compositions calculated for temperatures that range from 50 to 400 ºC, at 50°C increments. In each set, the thin dotted line represents mechanical mixing during Step 2. The thickness of the remaining lines increases with the degree of low-temperature basalt alteration, F, during Step 2. For readability, the reaction paths for which F=20% are represented by dashed lines. In subplot (d), the dashed-dotted horizontal black line represents mineral equilibrium.

Figure 4. Sulfate, Mg, K, and Si concentrations as functions of temperature during modeled reaction pathways at Kamaʻehuakanaloa. Seawater composition is shown with an open star and the solid black line represents Step 1 fluid compositions. The color gradation from purple to red represents families of paths for Step 2 fluid compositions originating with Step 1 fluid compositions calculated for temperatures that range from 50 to 400 ºC, at 50°C increments. In each set, the thin dotted line represents mechanical mixing during Step 2. The thickness of the remaining lines increases with the degree of low-temperature basalt alteration, F, during Step 2. For readability, the reaction paths for which F=20% are represented by dashed lines.

Figure 5. $H_2S$ and Fe concentrations as functions of temperature during modeled reaction pathways at Kamaʻehuakanaloa. The solid black line represents Step 1 fluid compositions. The color gradation from purple to red represents families of paths for Step 2 fluid compositions originating with Step 1 fluid compositions calculated for temperatures that range from 50 to 400 ºC, at 50°C increments. In each set, the thin dotted line represents mechanical mixing during Step 2. The thickness of the remaining lines increases with the degree of low-temperature basalt alteration, F, during Step 2. For readability, the reaction paths for which F=20% are represented by dashed lines.

Figure 6. Si, alkalinity, Ca, K and Fe concentrations as functions of pH values for 20-50 ºC vent fluids at Kamaʻehuakanaloa. The colored areas within the frame of each plot represent probability density functions of modeled compositions for vent fluids at the end of Step 2, when fluid mixtures reach

temperature between 50 and 20 ºC. Temperature maxima from 50 to 400 ºC during Step 1 are shown with color gradation from purple to red. Open symbols are for pre-eruptive vent-fluid compositions from Karl et al. (1988) and Sedwick et al. (1992) [squares and triangles, respectively]. The black contour lines within the frame of each panel indicate the probability density functions for post-eruptive vent-fluid compositions (Glazer and Rouxel, 2009; Rouxel et al., 2018). Closed circles show the SUBSEA data. The open star represents background seawater composition. Also shown along the top and right-hand side of each panel are projections of the same probability density functions onto the corresponding axes for each plot (a-h) for the SUBSEA data (dark grey) and modeled fluid compositions (colored according to Step 1 reaction temperature). Reaction conditions during Step 2 arise from mechanical mixing (left column: a, e, i, m, q) or equilibrium mixing with a degree of low-temperature basalt alteration, F, of 2%, 4% and 8% (2nd, 3rd and 4th column). Note the scale change from the 2nd column (F=2%) to the 3rd (F=4%) column for the panels showing Fe concentrations. The red box outlines the reaction conditions that are most consistent with our measured vent-fluid compositions.

Figure 1



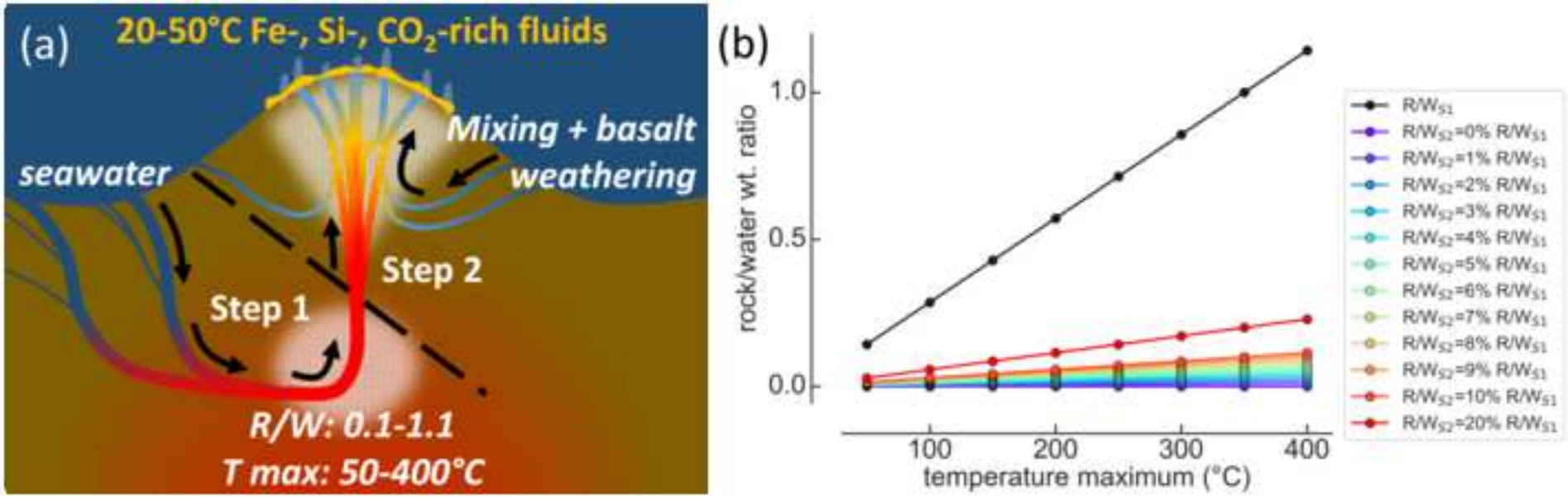

Figure 2

Click here to access/download;Figure;Figure2R2.png

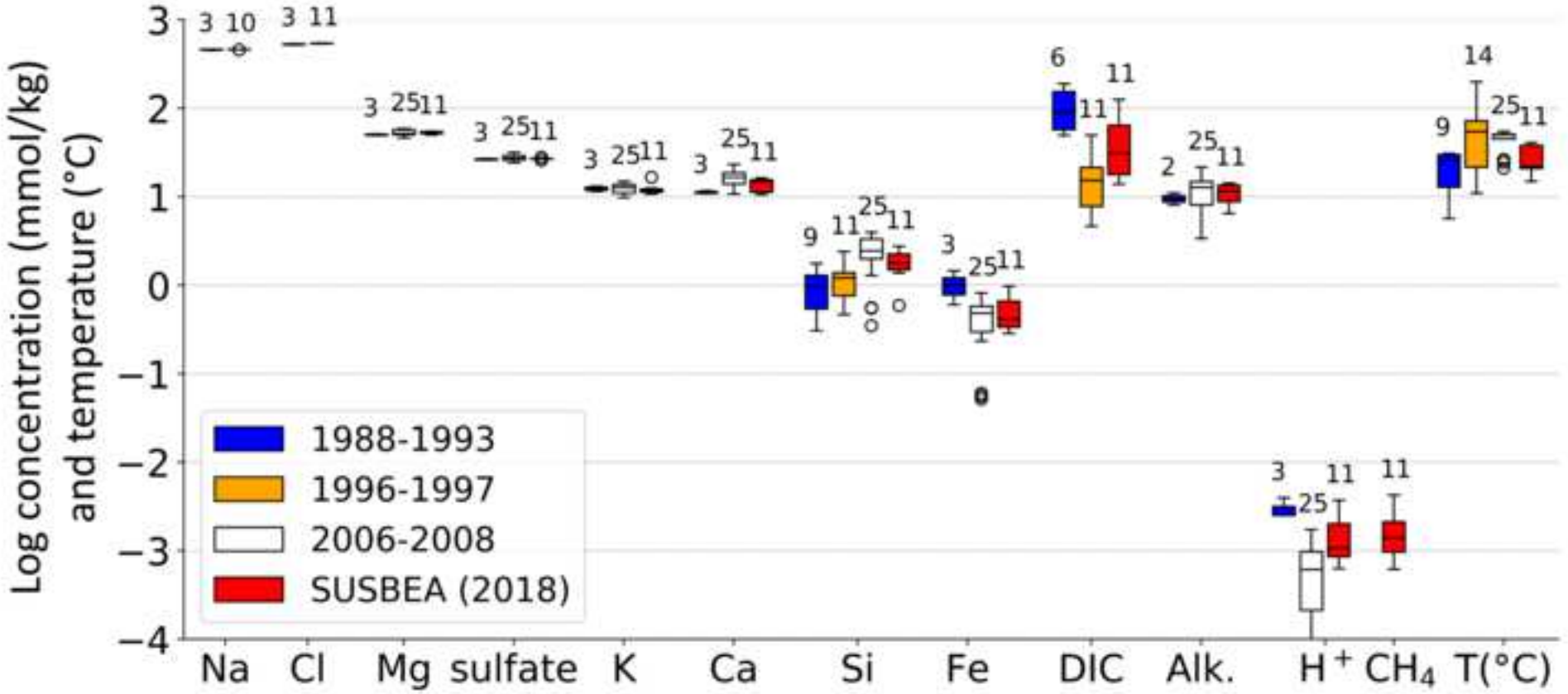

Figure 3

Click here to access/download;Figure;Figure3.png

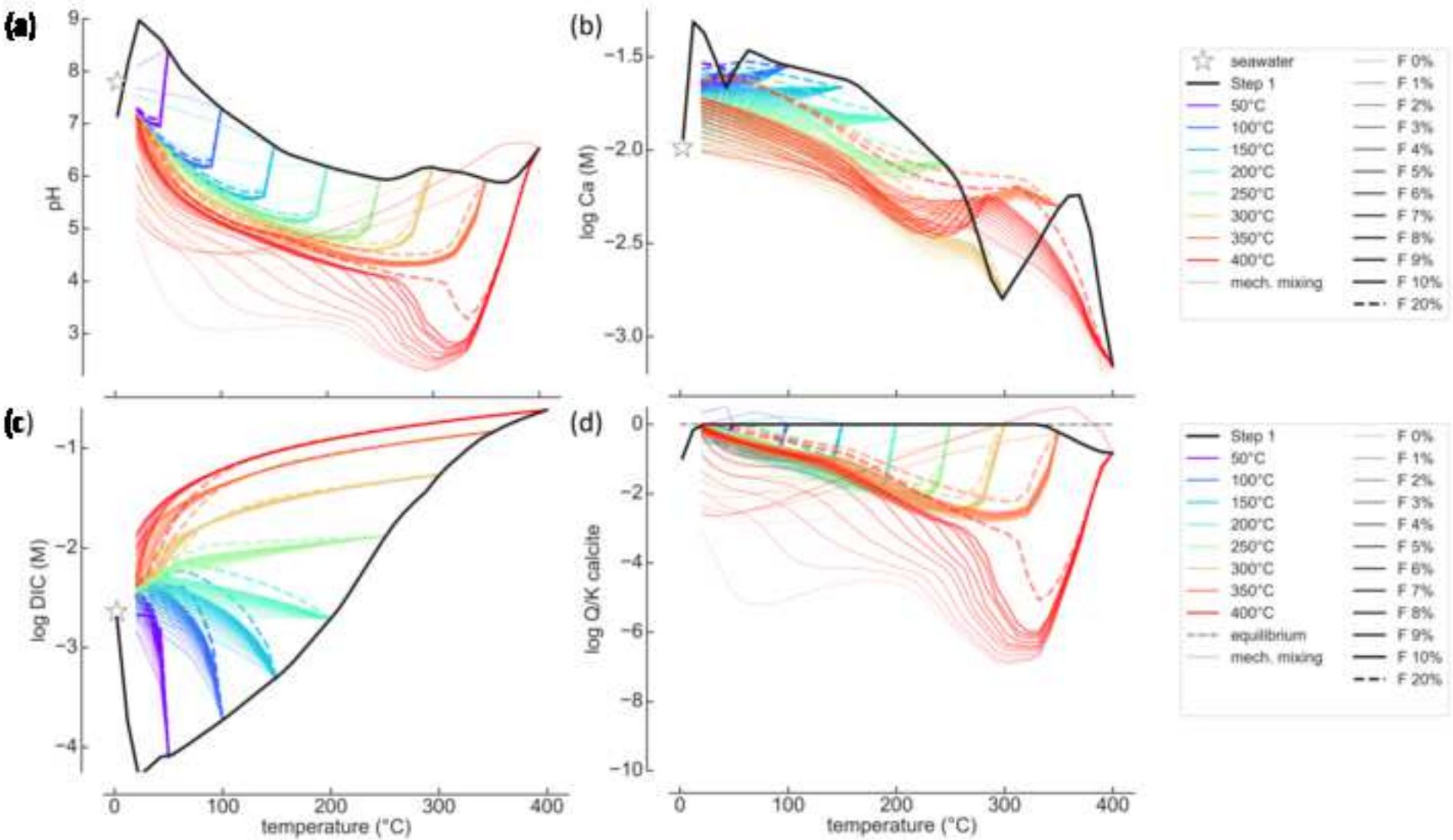

Figure 4

Click here to access/download;Figure;Figure4.png

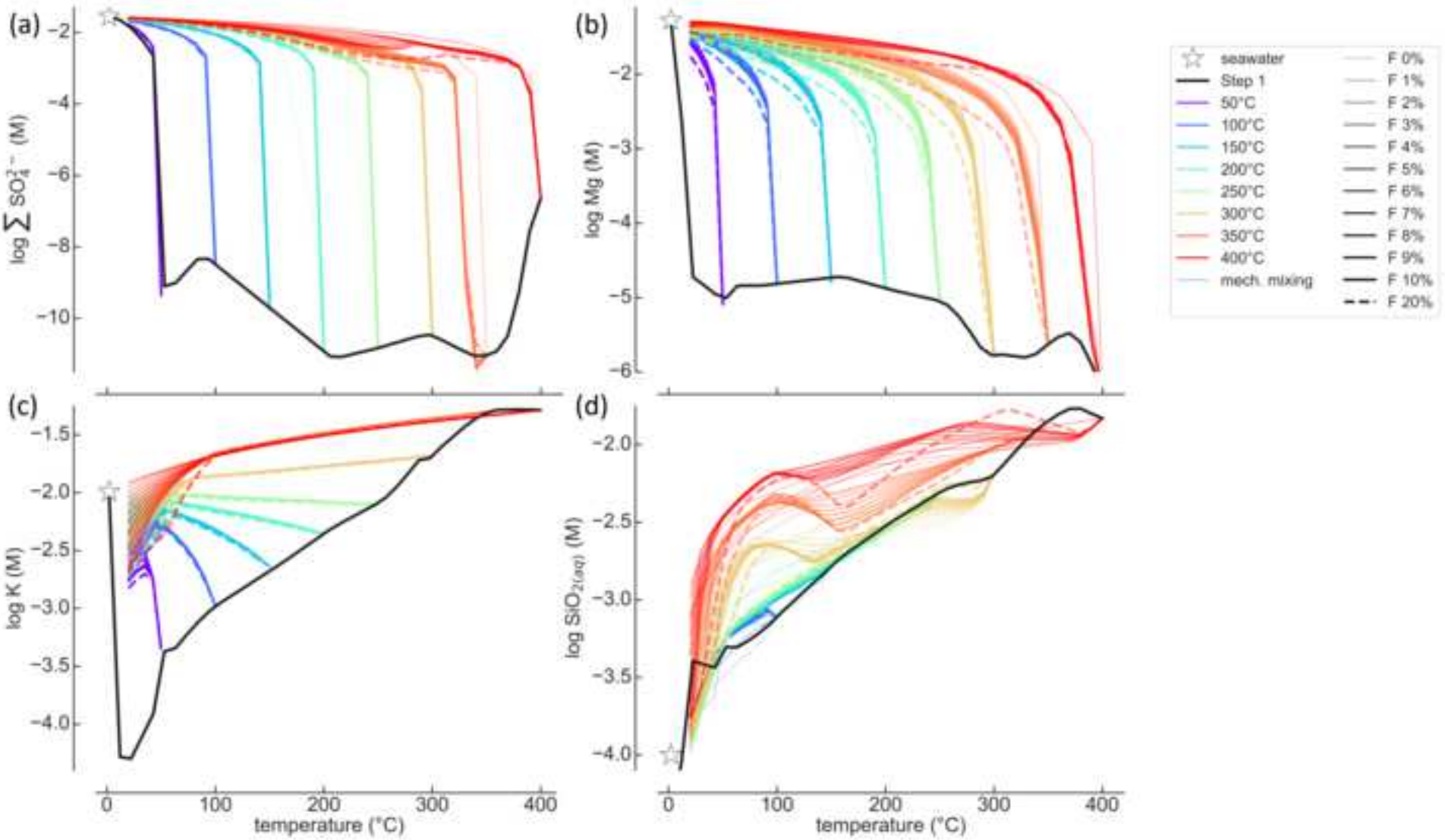

Figure 5

Click here to access/download;Figure;Figure5.png

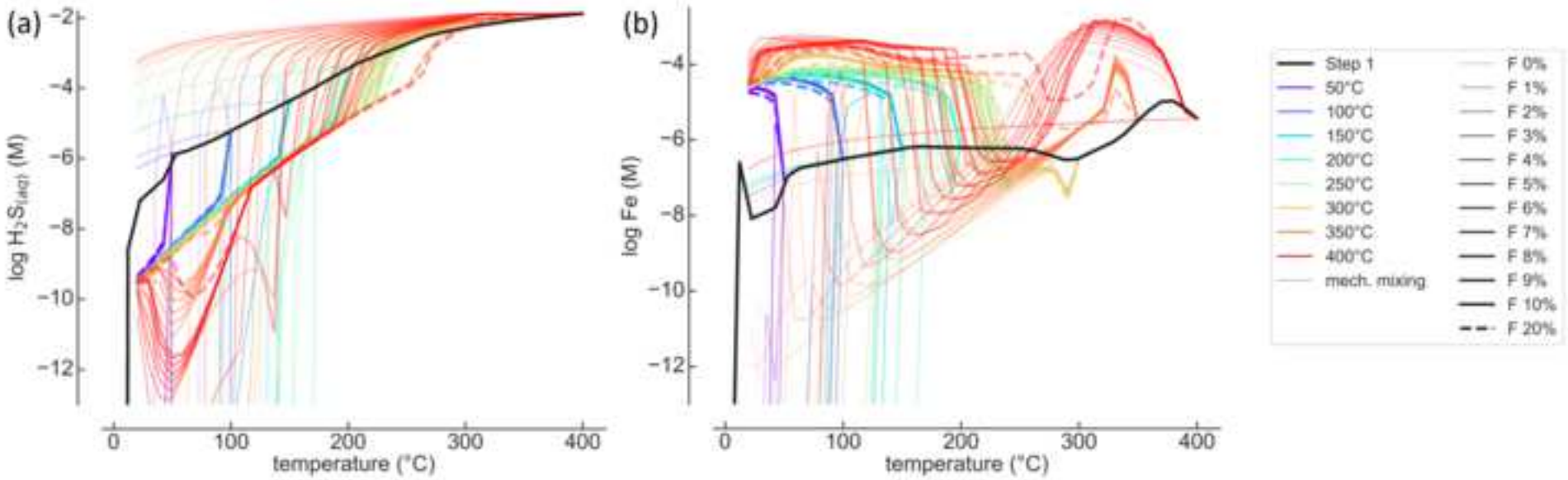

Figure 6

Click here to access/download;Figure;Figure6Alk.png